Appendix B

Supplementary Information for Chapter 3

B.1 Materials and Methods

B.1.1 General Considerations

All manipulations were carried out using standard Schlenk or glovebox techniques under an N_2 atmosphere. Solvents were deoxygenated and dried by thoroughly sparging with N_2, followed by passage through an activated alumina column in a solvent purification system by SG Water, USA LLC. Nonhalogenated solvents were tested with sodium benzophenone ketyl in tetrahydrofuran (THF) to confirm the absence of oxygen and water. Deuterated solvents were purchased from Cambridge Isotope Laboratories, Inc., degassed, and dried over activated 3-Å molecular sieves prior to use. [FeCN],[1] [$FeCNH_2$]$BAr^F{}_4$,[1] [FeCN][Na(12-c-4)$_2$],[1] [FeCNH]$BAr^F{}_4$,[1] [FeCNMe],[2] [$H(OEt_2)_2$]$BAr^F{}_4$,[3] $^{Me4}Cp_2Co$,[4] and triflate acids ([AH]OTf)[5] and [$BAr^F{}_4$] acids ([AH]$BAr^F{}_4$)[6] were synthesized using literature methods. $(C_6H_6)_2Cr$, Cp^*_2Cr and Cp_2Co, Cp_2Cr, Cp^*_2Co, $^{Et}Cp_2Co$ were purchased from Strem and used without further purification. All bases were purchased from Sigma and purified before use, liquid bases (aniline, lutidine, collidine, pyrrolidine, triethylamine, tetramethylguanidine) were distilled, solid anilines (2-chloroaniline, 4-chloroaniline and diphenylamine) were sublimed and triazabicyclodecene was recrystallized from by cooling a saturated Et_2O solution to -35°C and decanting.

B.1.2 Physical Methods

NMR: Nuclear Magnetic Resonance (NMR) measurements were recorded with a Varian 400 MHz spectrometer. ^{1}H NMR chemical shifts are reported in ppm relative to tetramethylsilane, using ^{1}H resonances from residual solvent as internal standards.[7]

UV-Vis: Ultraviolet-visible (UV-vis) absorption spectroscopy measurements were collected with a Cary 50 UV-vis spectrophotometer using a 1 cm path length quartz cuvette. All samples had a blank sample background subtraction applied. Temperature regulation for UV-Vis measurements was carried out with a Unisoku cryostat. Time course UV-Vis spectra were collected with the Scanning Kinetics application of the Cary WinUV software.

Mössbauer spectra: Mössbauer spectra were recorded on a spectrometer from SEE Co. (Edina, MN) operating in the constant acceleration mode in a transmission

geometry. The sample was kept in an SVT-400 cryostat form Janis (Wilmington, MA). The quoted isomer shifts are relative to the centroid of the spectrum of a metallic foil of α-Fe at room temperature (RT). Solution samples were transferred to a sample cup, freeze-quenched with liquid nitrogen inside the glovebox, and then immersed in liquid N_2 until mounted in the cryostat. Data analysis was performed using version 4 of the program WMOSS (www.wmoss.org) and quadrupole doublets were fit to Lorentzian lineshapes.

EPR Spectroscopy: X-band EPR spectra were obtained on a Bruker EMX spectrometer. Samples were collected at powers of 2 mW with modulation amplitudes of 4.00 G, modulation frequencies of 100.00 kHz, over a range of 1800 to 4500 Gauss. Spectra were baseline corrected. EPR spectra were modeled using the easyspin program.[8]

IR Spectroscopy: Infrared measurements were obtained on a Bruker Alpha spectrometer equipped with a diamond ATR probe (solid state) or in the liquid state in a cell with KBr windows.

X-Ray Crystallography: XRD studies were carried out at the Beckman Institute Crystallography Facility on a Brüker Kappa Apex II diffractometer (Mo Kα radiation). Structures were solved using SHELXS or SHELXT and refined against F2 on all data by full-matrix least squares with SHELXL. The crystals were mounted on a glass fiber under Paratone N oil.

B.2 Experimental procedures

B.2.1 Direct generation of $[FeCN\cdots HTBD]^0$

To confirm the assignment of the reaction of [FeCN] + Cp^*_2Co + $[TBDH]BAr^F_4$ as an H-bonded adduct, $[FeCN\cdots HTBD]^0$ we developed the direct synthesis of this species.

A solution of $[FeCN][Na(12\text{-}c\text{-}4)_2]$ (20 mg, 19 μmol) in 1 mL THF was cooled to −78°C and [TBDH]OTf (5.5 mg, 19 μmol) in 0.5 mL was added dropwise. The solution was allowed to stir for 30 minutes, after which it was filtered into and layered with pentane. All operations were done in the cold-well using pre-cooled glassware and solvent. Upon storage at −35°C overnight, dark orange crystals formed. However, substantial amounts of a red

complex (assumed [FeCN]) were also observed. Still, crystals sufficient for XRD could be selected, allowing crystallographic analysis.

B.2.2 Stepwise generation of [FeCNH$_2$]

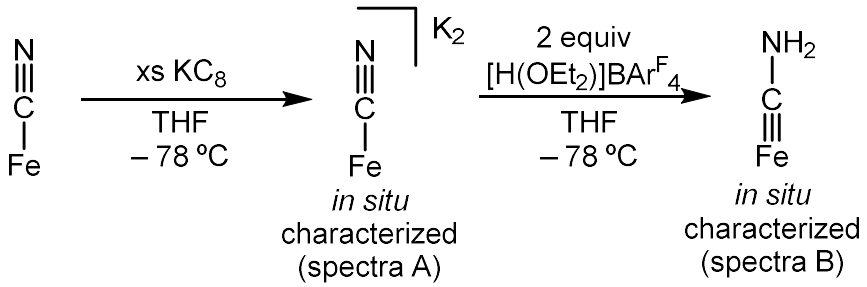

B.2.2.1 Generation of Mössbauer sample

[FeCN] (20 mg, 29 μmol) was dissolved in 0.5 mL THF in a 20 ml vial. The solution was cooled to −78 °C, and excess KC_8 was added. The reaction mixture was then filtered through a pipette loaded with filter paper, cellite, and KC_8 3xtimes to form. The reaction mixture was filtered to remove graphite and excess KC_8 to give a jet-black solution. This *in situ* formed material was used directly to form [FeCNH$_2$]. Alternatively, transferring this solution to a Mössbauer cup while maintaining the temperature, freezing the reaction mixture at 77 K, and analyzing by ^{57}Fe Mössbauer revealed a Mössbauer spectrum with parameters $\delta = 0.20$ mm s^{-1}, $\Delta E_Q = 0.18$ mm s^{-1} (Figure B.54A), with a minor impurity.

For generation of [FeCNH$_2$], 2 equiv [H(OEt$_2$)$_2$]BAr$^F_4$ (59 mg, 58 μmol) dissolved in 0.3 mL THF, was added slowly to *in situ* formed [FeCN]K$_2$, with an orange solution formed. Transferring this solution to a Mössbauer cup while maintaining the temperature, freezing the reaction mixture at 77 K, and analyzing by ^{57}Fe Mössbauer revealed a Mössbauer spectrum with parameters $\delta = 0.02$ mm s^{-1}; $\Delta E_Q = 0.96$ mms^{-1} (Figure B.54B), with some oxidized material also formed. The parameters of the major species fit those observed for [FeCNH$_2$] synthesized with [Ph$_2$NH$_2$]BAr$^F_4$ and Cp$_2$Co.

B.2.2.2 Generating UV-vis sample of [FeCNH$_2$]

[FeCN] (1 mg, 1.4 μmol) was dissolved in 2 mL THF in a 20 ml vial. The solution was cooled to −78 °C, and excess KC_8 was added. The reaction mixture was then filtered through a pipette loaded with filter paper, cellite, and KC_8 3xtimes to form. The reaction mixture was filtered to remove graphite and excess KC_8 to give a jet-black solution. This *in*

situ formed material was transferred to a cuvette, which was sealed with a septum. The cuvette was transferred out of the glovebox into a pre-cooled UNISOKO apparatus at −80°C and kept air-free by continuous purging by an N_2 needle.

For generation of [FeCNH$_2$], 2 equiv [H(OEt$_2$)$_2$]BAr$^F_4$ (2.9 mg, 2.8 μmol) dissolved in 0.5 mL THF, was added slowly to *in situ* formed [FeCN]K$_2$, with an orange solution formed (see Figure B.24). Addition of a third equivalent [H(OEt$_2$)$_2$]BAr$^F_4$ resulted in clean oxidation to [FeCNH$_2$]$^+$, with characteristic peaks at 900 nm and 520 nm.

B.2.3 Attempts to generate [FeCNH]

B.2.3.1 Reduction of [FeCNH]$^+$

A solution of [^{57}FeCNH]BAr$^F_4$ (3 mg, 2.1 μmol) was dissolved in 0.5 mL 2-MeTHF and cooled to −115°C. Cp*$_2$Cr (0.6 mg, 2.1 μmol) in 0.2 mL 2-MeTHF was added, and the solution was allowed to stir for 1 minute, rapidly transferred to a pre-cooled Mössbauer cup, and frozen to 77 K. The resulting Mössbauer sample was loaded and analyzed, showing a 1:1 mixture of [FeCN] and [FeCNH$_2$] (see Figure B.56).

B.2.3.2 Protonation of [FeCN][Na(12-c-4)$_2$]

A solution of [^{57}FeCN][Na(12-c-4)$_2$] (2 mg, 1.9 μmol) was dissolved in 0.5 mL 2-MeTHF and cooled to −115°C. [H(OEt$_2$)$_2$]BAr$^F_4$ (1.9 mg, 1.9 μmol) in 0.2 mL 2-MeTHF was added, the solution was allowed to stir for 1 minute, rapidly transferred to a pre-cooled Mössbauer cup and frozen to 77 K. The resulting Mössbauer sample was loaded and analyzed, showing a 1:1 mixture of [FeCN] and [FeCNH$_2$], as well as some unreacted starting material (see Figure B.55).

B.2.3.3 Deprotonation of [FeCNH$_2$][BAr$^F_4$]

A solution of [FeCNH$_2$][BAr$^F_4$] (2 mg, 1.9 μmol) was dissolved in 2.5 mL 2-MeTHF, added to a cuvette that was sealed with a septum, brought out of the glovebox, into a pre-cooled UNISOKO apparatus and cooled to −130°C. NEt$_3$ (1 mg, 1.5 μl, 9.5 μmol) in 0.5 mL 2-MeTHF was added. Analysis by UV-vis showed peaks consistent with the formation of [FeCN] and [FeCNH$_2$] (see Figure B.25).

B.3 UV-vis spectroscopy

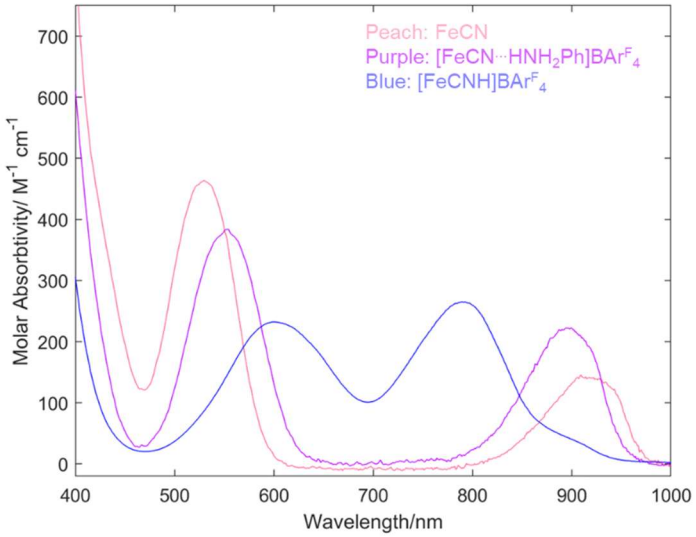

Figure B.1. UV-vis spectra of [FeCN···HNH_2Ph]BAr^F_4 compared to [FeCN], [FeCNH]BAr^F_4.

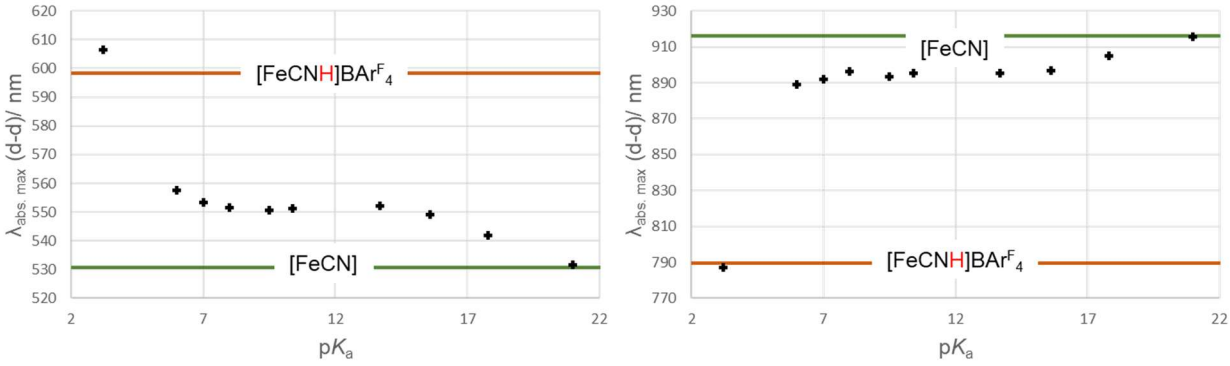

Figure B.2. Shift in position of d-d transition of UV-vis maxim upon varying acid strength, solid lines represent [FeCN] (green) and [FeCNH]BAr^F_4 (orange).

B.3.1 Titrations demonstrating reversible interconversion of [FeCN] and [$FeCNH_2$]

B.3.1.1 Oxidation of [$FeCNH_2$]

A cuvette with [$FeCNH_2$] (2 mg, 2.9 μmol) was generated at −80 °C (see section S2.3.2), sealed with a septum, with a N_2 needle constantly purging to ensure an air-free system. Lut (3 equiv, 0.9 mg, 8.7 μmol) in 0.5 mL THF was added via syringe. Then [Cp^*_2Cr][BAr^F_4] (3 equiv, 10.3 mg, 8.7 μmol) in 0.5 mL was titrated via syringe with

spectrum collected between every addition of oxidant, with peaks consistent with [FeCNH$_2$] disappearing and [FeCN] forming. THF had to be used to generate [FeCNH$_2$]; attempts using Et$_2$O were unsuccessful due to the low solubility of [FeCN]K$_2$ under these conditions.

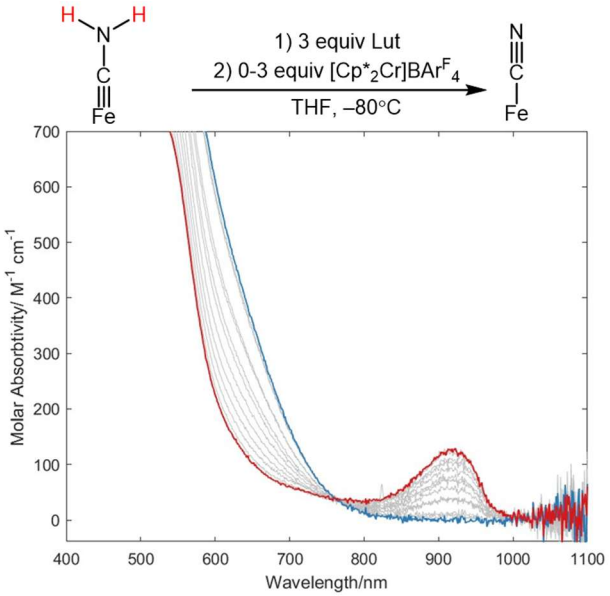

Figure B.3. UV-vis titration of [Cp*$_2$Cr]BAr$^F_4$ (3 equiv per Fe) into mixture of [FeCNH$_2$] (1.2 mM) and Lut (3 equiv per Fe) (Blue) in THF at −80°C. The final trace (Red) shows consumption of [FeCNH$_2$] and formation of [FeCN].

B.3.1.2 Reduction of [FeCN]

A cuvette was loaded [FeCN] (2.5 mg, 3.6 µmol) in 3 mL THF with [PhNH$_3$]BAr$^F_4$ (3 equiv, 10.6 mg, 10.8 µmol) at −80 °C sealed with a septum, with a N$_2$ needle constantly purging to assure an air-free system. To this, Cp*$_2$Cr (3 equiv, 3.5 mg, 10.8 µmol) in 0.5 mL was titrated via syringe with a spectrum collected between every addition of reductant, with peaks consistent with [FeCN] disappearing and [FeCNH$_2$] forming. THF had to be used to generate [FeCNH$_2$].

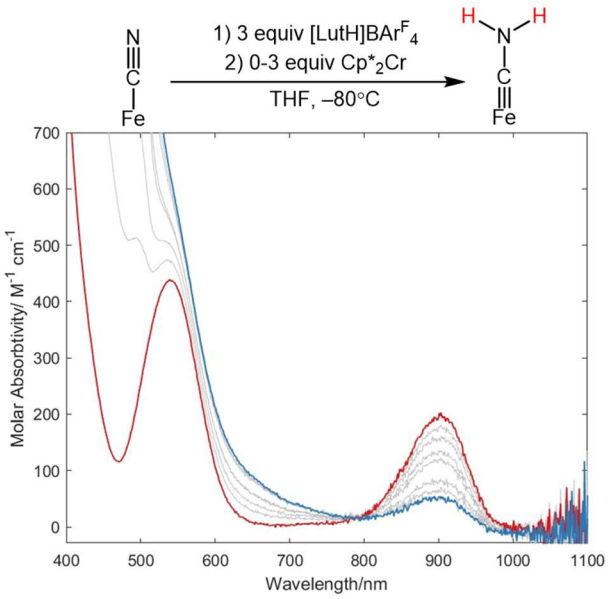

Figure B.4. UV-vis titration of [Cp*$_2$Cr] (3 equiv per Fe) into mixture of [FeCN] (1.2 mM) and [LutH]BAr$^F_4$ (3 equiv per Fe) (Red) in THF at −80°C. The final trace (Blue) shows consumption of [FeCN] and formation of [FeCNH$_2$].

B.3.2 Generation of Pourbaix diagram

B.3.2.1 General procedure

A cuvette was loaded with [FeCN] (1.25 mM) in Et$_2$O and sealed with a septum inside the glovebox. The cuvette was then taken out of the glovebox and loaded into a UNISOKO cooling apparatus connected to the UV-vis. The cuvette was cooled to −80°C and allowed to equilibrate for at least 10 minutes. Spectra were typically collected every minute while equilibrating to ensure no ice formation on the cuvette. The system was kept air-free by an N$_2$ needle through the septa. Acid [HA]BAr$^F_4$ (2.5 equiv) in 0.5 mL Et$_2$O was added via syringe, and the reaction was allowed to equilibrate for an additional 5 minutes. Reductant (2.5 equiv) was then added via syringe, and the reaction was monitored by UV-vis.

Products were assigned by comparing the spectra to known spectra of [FeCNH$_2$]$^+$, [FeCN], [FeCNH]$^+$ and [FeCNH$_2$]. In addition, when uncertain, ^{57}Fe Mössbauer, cw-EPR, and reductant titrations were used to aid the assignment. The reagent strengths are presented in Table B.2, along with the observed products formed. The driving force for [Fe]-products

based on previous thermochemistry,[2] is presented in Table B.2. The individual UV-vis spectra are presented in Figures B.5-B.23 and Table B.1.

B.3.3.2 Thermodynamic considerations for Pourbaix diagram

For the generation of the Pourbaix diagram (Figure 3.5), the general procedure and summary of resulting products are provided in section 3.3. In Figure 3.5, the lines provide the predicted products. To supplement this analysis, we provide a Table B.2 which shows the ΔG (kcal mol-1) for the formation of the 4 products formed, $[FeCNH_2]$, $[FeCNH]^+$, $[FeCN]^-$ and $[FeCNH_2]^+$ given by equations B.1-B.4. If all products are disfavored, [FeCN] (or $[FeCN]^{\cdots}HA^+$) is the predicted product.

For a given reductant $E(red^{+/0})$ and acid (pK_a), $BDFE_{eff}$ is given by:

$$BDFE_{eff} = 23.06\ E(red^{+/0}) + 1.37\ pK_a(acid) + C_G \quad \text{(eqn B.1)}$$

where $C_G = 59.9$ kcal mol^{-1} in THF

Based on the thermochemistry of $[FeCNH_x]$ (main text Figure 3.5)[2] the ΔG (kcal mol^{-1}) for various products is as follows:

$$\Delta G(FeCNH_2) = 2*(BDFE_{eff} - 39) \text{ (eqn B.2)}$$

$$\Delta G(FeCNH^+) = 1.37(pK_a(acid) - 5.6) \text{ (eqn B.3)}$$

$$\Delta G(FeCN^-) = 23.06(E(red^{+/0}) - 2.1\ V) \text{ (eqn B.4)}$$

$$\Delta G(FeCNH_2^+) = 1.37(pK_a(acid) - 7.1) + (BDFE_{eff} - 38) \text{ (eqn B.5)}$$

Table B.1. Summary of product formation studies varying acid and reductant for [FeCN] reduction, reduction potential, and acid used to calculate $BDFE_{eff}$ and ΔG using eqn B.1-B.4.

Reductant (V vs $Fc^{+/0}$)	Acid (pK_a in THF)	$BDFE_{eff}$ (kcal mol^{-1})	ΔG (kcal mol^{-1})	Products
Cp_2Cr (−1.11)	$[^{2\text{-Cl}}PhNH_3]BAr^F{}_4$ (5.6)	42.0	5.4	$[FeCN\cdots HA]^+$
Cp_2Cr (−1.11)	$[^{4\text{-Cl}}PhNH_3]BAr^F{}_4$ (5.6)	43.9	9.2	$[FeCN\cdots HA]^+$
$(C_6H_6)_2Cr$ (−1.22)	$[Ph_2NH_2]BAr^F{}_4$ (3.2)	36.2	-6.3	$[FeCNH_2]^+$
$(C_6H_6)_2Cr$ (−1.22)	$[^{2\text{-Cl}}PhNH_3]BAr^F{}_4$ (5.6)	39.4	0.3	$[FeCNH_2]^+$
$(C_6H_6)_2Cr$ (−1.22)	$[^{4\text{-Cl}}PhNH_3]BAr^F{}_4$ (7.0)	41.4	2.2	$[FeCN]\leftrightarrow[FeCNH_2]^+$
Cp_2Co (−1.33)	$[Ph_2NH_2]BAr^F{}_4$ (3.2)	33.6	-11.4	$[FeCNH_2]$
Cp_2Co (−1.33)	$[^{4\text{-Cl}}PhNH_3]BAr^F{}_4$ (7.0)	38.8	-1.0	$[FeCN]\leftrightarrow[FeCNH_2]$
Cp_2Co (−1.33)	$[PhNH_3]BAr^F{}_4$ (8.0)	40.2	1.8	$[FeCN]\leftrightarrow[FeCNH_2]$
Cp_2Co (−1.33)	$[LutH]BAr^F{}_4$ (9.5)	42.2	5.9	$[FeCN\cdots HA]^+$
$Cp^*{}_2Cr$ (−1.47)	$[PhNH_3]BAr^F{}_4$ (8.0)	37.0	-4.7	$[FeCNH_2]$
$Cp^*{}_2Cr$ (−1.47)	$[LutH]BAr^F{}_4$ (9.5)	39.0	-0.6	$[FeCN]\leftrightarrow[FeCNH_2]$
$Cp^*{}_2Cr$ (−1.47)	$[ColH]BAr^F{}_4$ (10.4)	40.2	1.9	$[FeCN]\leftrightarrow[FeCNH_2]$
$Cp^*{}_2Cr$ (−1.47)	$[Et_3NH]BAr^F{}_4$ (13.7)	44.8	10.9	$[FeCN\cdots HA]^+$
$^{Me4}Cp_2Co$ (−1.76)	$[Et_3NH]BAr^F{}_4$ (13.7)	38.1	-2.4	$[FeCNH_2]$
$^{Me4}Cp_2Co$ (−1.76)	$[pyrrH]BAr^F{}_4$ (15.6)	40.7	2.8	$[FeCN]\leftrightarrow[FeCNH_2]$
$^{Me4}Cp_2Co$ (−1.76)	$[TMGH]BAr^F{}_4$ (17.8)	43.7	8.8	$[FeCN\cdots HA]^+$
$Cp^*{}_2Co$ (−1.94)	$[pyrrH]BAr^F{}_4$ (15.6)	36.5	-5.5	$[FeCNH_2]$
$Cp^*{}_2Co$ (−1.94)	$[TMGH]BAr^F{}_4$ (17.8)	39.5	0.5	$[FeCN\cdots HTMG]^0$
$Cp^*{}_2Co$ (−1.94)	$[TBDH]BAr^F{}_4$ (21.0)	43.9	9.3	$[FeCN\cdots HTBD]^0$

Table B.2. Thermodynamics of [Fe]-product formations for [FeCN] reduction, using different acids and reductants and eqn B.2-B.5

Reductant (V vs $Fc^{+/0}$)	Acid (pK_a in THF)	ΔG (kcal mol^{-1}) for products			
		$[FeCNH_2]$	$[FeCNH]^+$	$[FeCN]^-$	$[FeCNH_2]^+$
Cp_2Cr (−1.11)	$[^{2\text{-Cl}}PhNH_3]BAr^F_4$ (5.6)	5.4	0.0	22.1	2.6
Cp_2Cr (−1.11)	$[^{4\text{-Cl}}PhNH_3]BAr^F_4$ (5.6)	9.2	1.9	22.1	6.4
$(C_6H_6)_2Cr$ (−1.22)	$[Ph_2NH_2]BAr^F_4$ (3.2)	-6.3	-3.3	19.6	-6.5
$(C_6H_6)_2Cr$ (−1.22)	$[^{2\text{-Cl}}PhNH_3]BAr^F_4$ (5.6)	0.3	0.0	19.6	0.0
$(C_6H_6)_2Cr$ (−1.22)	$[^{4\text{-Cl}}PhNH_3]BAr^F_4$ (7.0)	4.1	1.9	19.6	3.9
Cp_2Co (−1.33)	$[Ph_2NH_2]BAr^F_4$ (3.2)	-11.4	-3.3	17.1	-9.1
Cp_2Co (−1.33)	$[^{4\text{-Cl}}PhNH_3]BAr^F_4$ (7.0)	-1.0	1.9	17.1	1.3
Cp_2Co (−1.33)	$[PhNH_3]BAr^F_4$ (8.0)	1.8	3.3	17.1	4.1
Cp_2Co (−1.33)	[LutH]BAr^F_4 (9.5)	5.9	5.3	17.1	8.2
Cp^*_2Cr (−1.47)	$[PhNH_3]BAr^F_4$ (8.0)	-4.7	3.3	13.8	0.8
Cp^*_2Cr (−1.47)	[LutH]BAr^F_4 (9.5)	-0.6	5.3	13.8	5.0
Cp^*_2Cr (−1.47)	[ColH]BAr^F_4 (10.4)	1.9	6.6	13.8	7.4
Cp^*_2Cr (−1.47)	$[Et_3NH]BAr^F_4$ (13.7)	10.9	11.1	13.8	16.5
$^{Me4}Cp_2Co$ (−1.76)	$[Et_3NH]BAr^F_4$ (13.7)	-2.4	11.1	7.1	9.8
$^{Me4}Cp_2Co$ (−1.76)	[pyrrH]BAr^F_4 (15.6)	2.8	13.7	7.1	15.0
$^{Me4}Cp_2Co$ (−1.76)	[TMGH]BAr^F_4 (17.8)	8.8	16.7	7.1	21.0
Cp^*_2Co (−1.94)	[pyrrH]BAr^F_4 (15.6)	-5.5	13.7	3.0	10.8
Cp^*_2Co (−1.94)	[TMGH]BAr^F_4 (17.8)	0.5	16.7	3.0	16.9
Cp^*_2Co (−1.94)	[TBDH]BAr^F_4 (21.0)	9.3	21.1	3.0	25.6

S3.3.3 UV-vis spectra of reactions of [FeCN] with acid and reductant

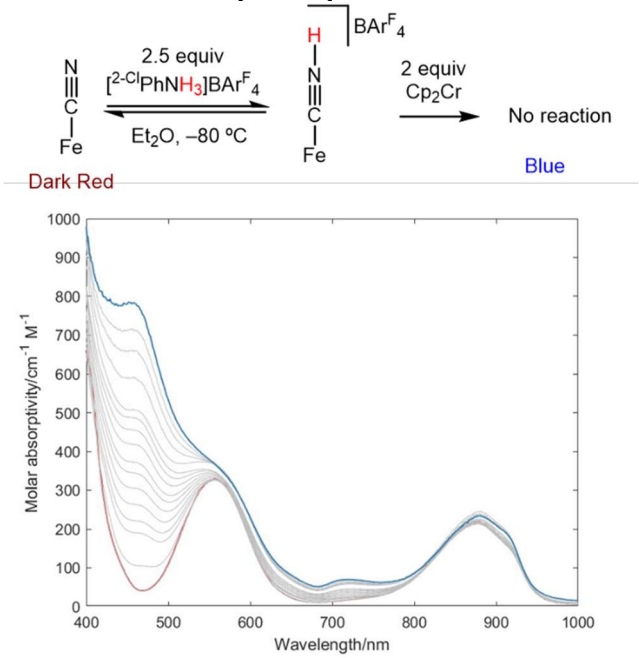

Figure B.5. UV-vis titration of Cp_2Cr (2.5 equiv per Fe) into mixture of [FeCN] (1.2 mM) and $[^{2\text{-Cl}}PhNH_3]BAr^F{}_4$ (2.5 equiv per Fe) (Red) in Et_2O at −80°C. The final trace (Blue) shows no consumption of [FeCN] starting material.

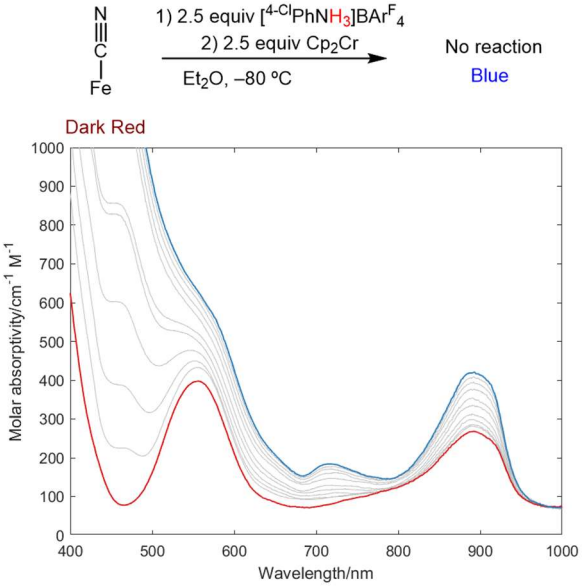

Figure B.6. UV-vis titration of Cp_2Cr (2.5 equiv per Fe) into mixture of [FeCN] (1.2 mM) and $[^{4\text{-Cl}}PhNH_3]BAr^F{}_4$ (2.5 equiv per Fe) (Red) in Et_2O at −80°C. The final trace (Blue) shows no consumption of [FeCN] starting material.

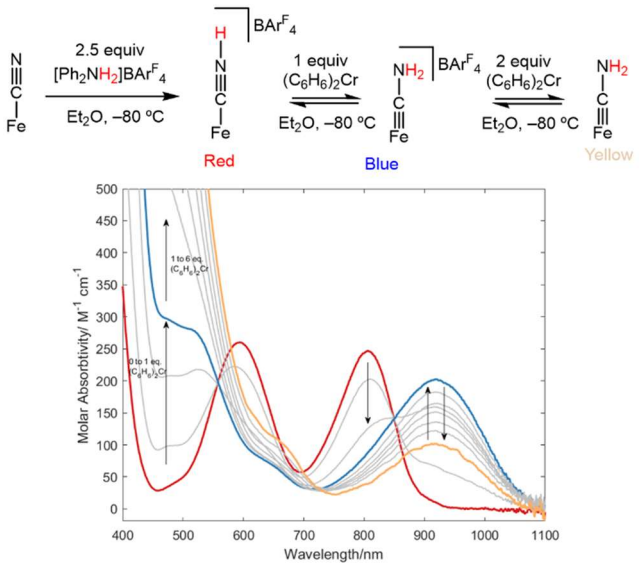

Figure B.7. UV-vis titration of $(C_6H_6)_2Cr$ (0-6 equiv per Fe) into mixture of [FeCN] (1.2 mM) and $[Ph_2NH_2]BAr^F{}_4$ (2.5 equiv per Fe) (Red) in Et_2O at −80°C. Initially, $[FeCNH_2]^+$ is formed. Upon addition of more equivalents of reductant, some $[FeCNH_2]$ begins to form.

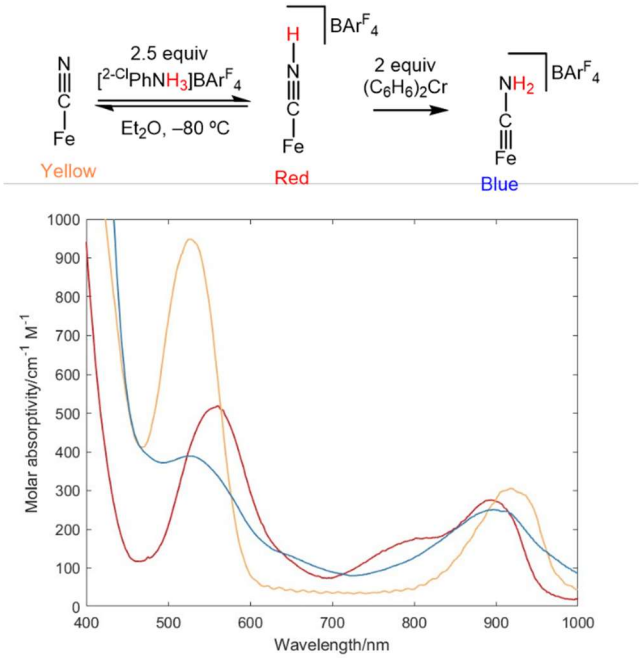

Figure B.8. UV-vis monitored addition of $(C_6H_6)_2Cr$ (2.5 equiv per Fe) into mixture of [FeCN] (1.2 mM) and $[^{2\text{-Cl}}PhNH_3]BAr^F{}_4$ (2.5 equiv per Fe) (Red) in Et_2O at −80°C. The final trace (Blue) shows consumption of [FeCN] and formation of $[FeCNH_2]^+$. Upon addition of acid to [FeCN] (yellow trace is without acid), a mixture of [FeCN]↔$[FeCNH]^+$ is established.

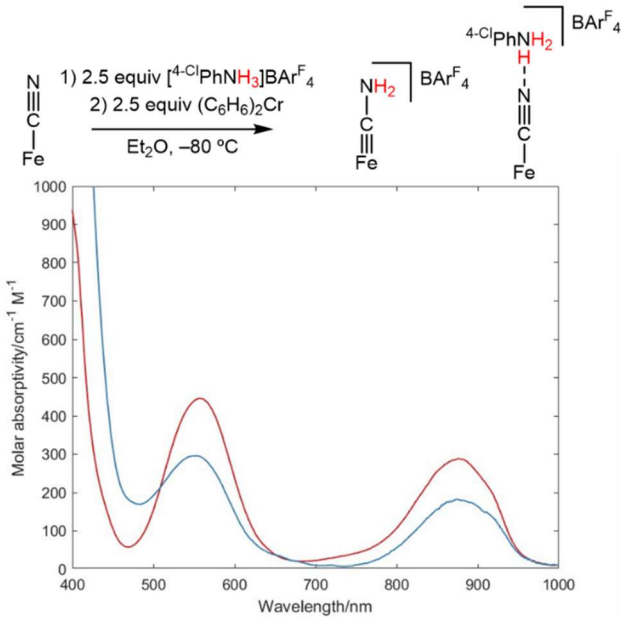

Figure B.9. UV-vis monitored addition of $(C_6H_6)_2Cr$ (2.5 equiv per Fe) into mixture of [FeCN] (1.2 mM) and $[^{4\text{-Cl}}PhNH_3]BAr^F{}_4$ (2.5 equiv per Fe) (Red) in Et_2O at −80°C. The final trace (Blue) shows partial consumption of [FeCN] and a mixture of $[FeCN]\leftrightarrow[FeCNH_2]^+$.

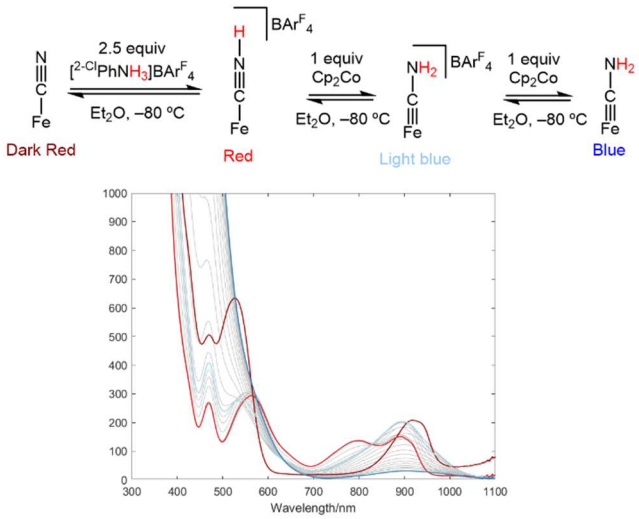

Figure B.10. UV-vis monitored titration of Cp_2Co (2.5 equiv per Fe) into mixture of [FeCN] (1.2 mM) and $[^{2\text{-Cl}}PhNH_3]BAr^F{}_4$ (2.5 equiv per Fe) (Red) in Et_2O at −80°C. The final trace (Blue) shows consumption of [FeCN] and formation of $[FeCNH_2]$. Upon addition of one equivalent of Cp_2Co (light blue trace), $[FeCNH_2]^+$ is formed. Upon addition of acid to [FeCN] (dark red trace is without acid), a mixture of $[FeCN]\leftrightarrow[FeCNH]^+$ is established.

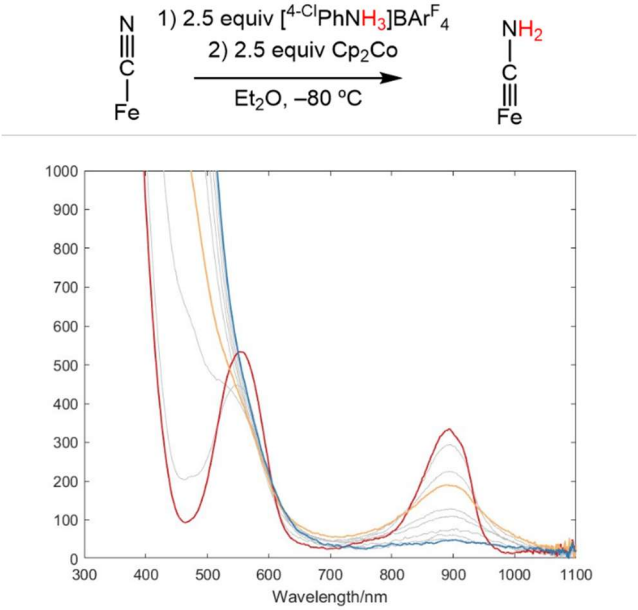

Figure B.11. UV-vis monitored titration of Cp_2Co (2.5 equiv per Fe) into mixture of [FeCN] (1.2 mM) and $[^{4\text{-Cl}}PhNH_3]BAr^F{}_4$ (2.5 equiv per Fe) (Red) in Et_2O at −80°C. The final trace (Blue) shows consumption of [FeCN] and formation of $[FeCNH_2]$. Upon addition of one equivalent of Cp_2Co (yellow trace), $[FeCNH_2]^+$ is formed.

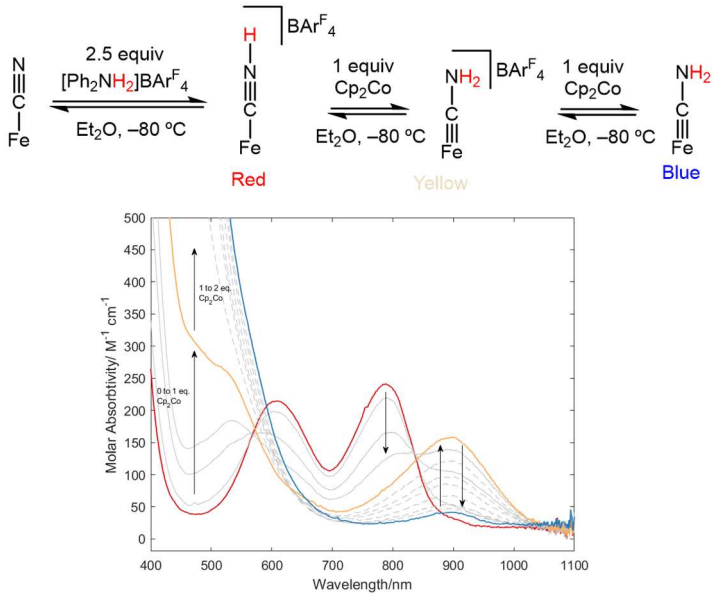

Figure B.12. UV-vis monitored titration of Cp_2Co (2.5 equiv per Fe) into mixture of [FeCN] (1.2 mM) and $[Ph_2NH_2]BAr^F{}_4$ (2.5 equiv per Fe) (Red) in Et_2O at −80°C. The final

trace (Blue) shows consumption of [FeCN] and formation of [$FeCNH_2$]. Upon addition of one equivalent of Cp_2Co (yellow trace), $[FeCNH_2]^+$ is formed.

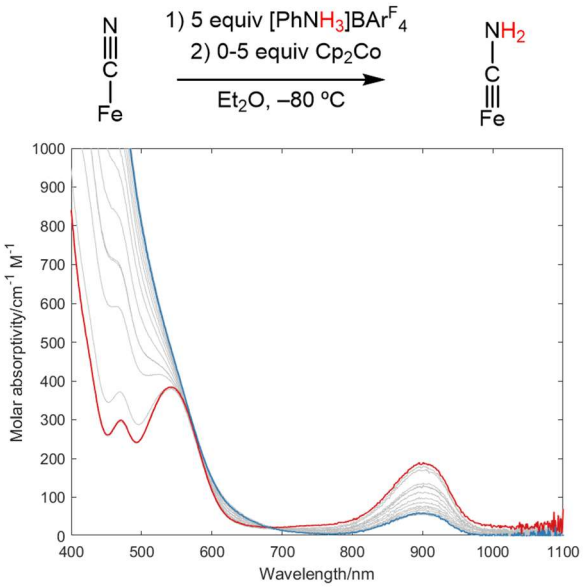

Figure B.13. UV-vis monitored titration of Cp_2Co (5 equiv per Fe) into mixture of [FeCN] (1.2 mM) and $[PhNH_3]BAr^F_4$ (5 equiv per Fe) (Red) in Et_2O at −80°C. The final trace (Blue) shows consumption of [FeCN] and partial formation of [$FeCNH_2$].

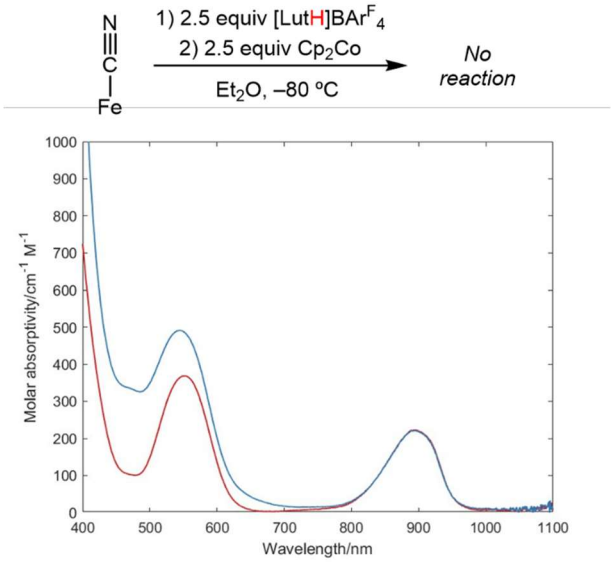

Figure B.14. UV-vis monitored addition of Cp_2Co (2.5 equiv per Fe) into mixture of [FeCN] (1.2 mM) and [LutH]BAr$^F_4$ (2.5 equiv per Fe) (Red) in Et_2O at −80°C. The final trace (Blue) shows no consumption of [FeCN].

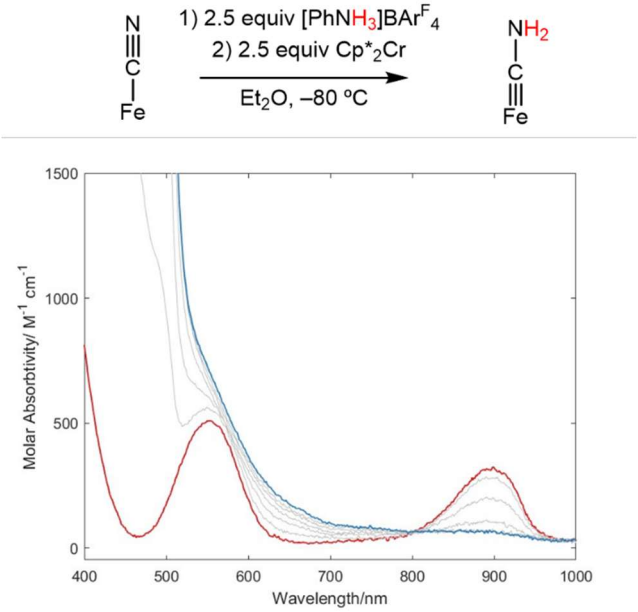

Figure B.15. UV-vis monitored titration of Cp*$_2$Cr (2.5 equiv per Fe) into mixture of [FeCN] (1.2 mM) and [PhNH$_3$]BAr$^F_4$ (2.5 equiv per Fe) (Red) in Et_2O at −80°C. The final trace (Blue) shows consumption of [FeCN] and formation of [FeCNH$_2$].

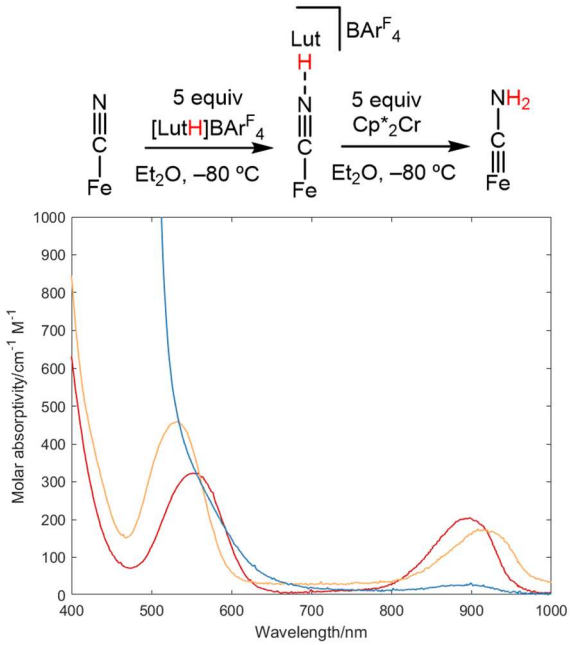

Figure B.16. UV-vis monitored addition of Cp*$_2$Cr (5 equiv per Fe) into mixture of [FeCN] (1.2 mM) and [LutH]BAr$^F_4$ (5 equiv per Fe) (Red) in Et$_2$O at −80°C. The final trace (Blue) shows formation of consumption of [FeCN] and formation [FeCNH$_2$]. Comparing [FeCN] before (yellow trace) and after addition of [LutH]BAr$^F_4$ shows changes similar to those observed upon addition of [PhNH$_3$]BAr$^F_4$, suggesting formation of an H-bond.

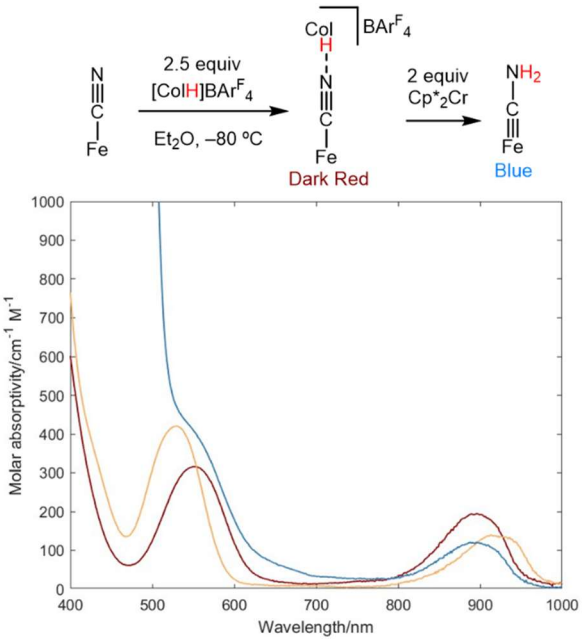

Figure B.17. UV-vis monitored addition of Cp*$_2$Cr (2.5 equiv per Fe) into mixture of [FeCN] (1.2 mM) and [ColH]BAr$^F_4$ (2.5 equiv per Fe) (Red) in Et$_2$O at −80°C. The final

trace (Blue) shows formation of partial consumption of [FeCN] and concomitant formation [$FeCNH_2$]. Comparing [FeCN] before (yellow trace) and after addition of [ColH]$BAr^F{}_4$ (dark red) shows changes similar to those observed upon addition of [$PhNH_3$]$BAr^F{}_4$, suggesting formation of an H-bond.

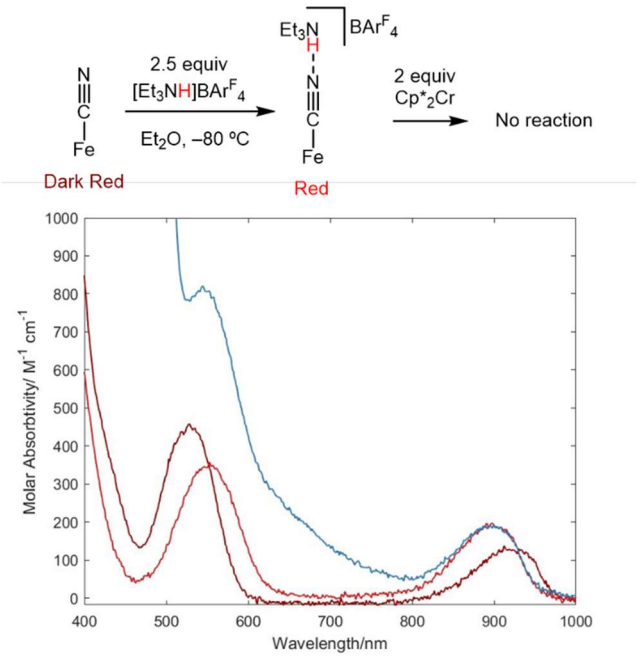

Figure B.18. UV-vis monitored addition of $Cp^*{}_2Cr$ (2.5 equiv per Fe) into mixture of [FeCN] (1.2 mM) and [Et_3NH]$BAr^F{}_4$ (2.5 equiv per Fe) (Red) in Et_2O at −80°C. The final trace (Blue) shows no consumption of [FeCN]. Comparing [FeCN] before (dark red trace) and after addition of [Et_3NH]$BAr^F{}_4$ shows changes similar to those observed upon addition of [$PhNH_3$]$BAr^F{}_4$, suggesting formation of an H-bond.

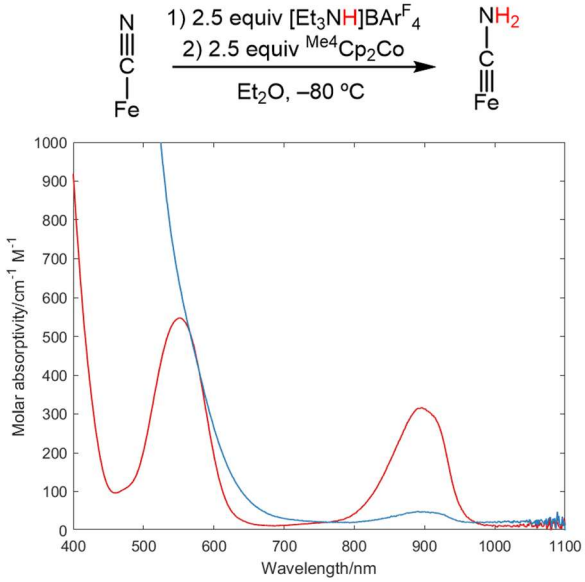

Figure B.19. UV-vis monitored addition of $^{Me4}Cp_2Co$ (2.5 equiv per Fe) into mixture of [FeCN] (1.2 mM) and $[Et_3NH]BAr^F{}_4$ (2.5 equiv per Fe) (Red) in Et_2O at −80°C. The final trace (Blue) shows consumption of [FeCN] and formation of $[FeCNH_2]$.

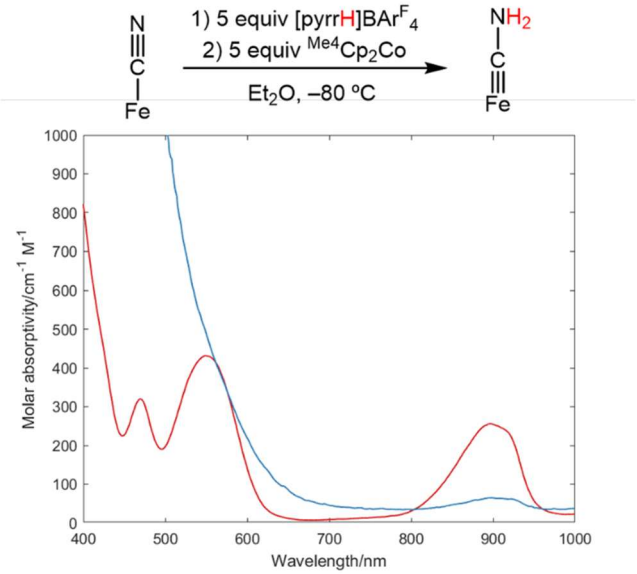

Figure B.20. UV-vis monitored addition of $^{Me4}Cp_2Co$ (2.5 equiv per Fe) into mixture of [FeCN] (1.2 mM) and $[pyrrH]BAr^F{}_4$ (2.5 equiv per Fe) (Red) in Et_2O at −80°C. The final trace (Blue) shows partial consumption of [FeCN] and concomitant formation $[FeCNH_2]$.

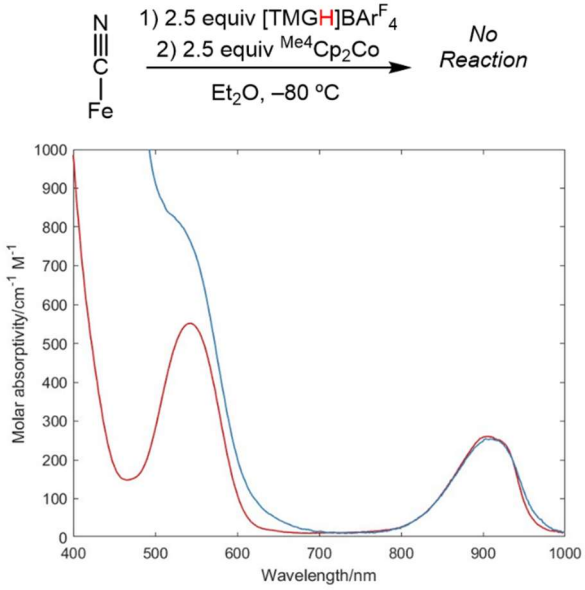

Figure B.21. UV-vis monitored addition of $^{Me4}Cp_2Cr$ (2.5 equiv per Fe) into mixture of [FeCN] (1.2 mM) and [TMGH]BAr$^F_4$ (2.5 equiv per Fe) (Red) in Et_2O at −80°C. The final trace (Blue) shows no consumption of [FeCN].

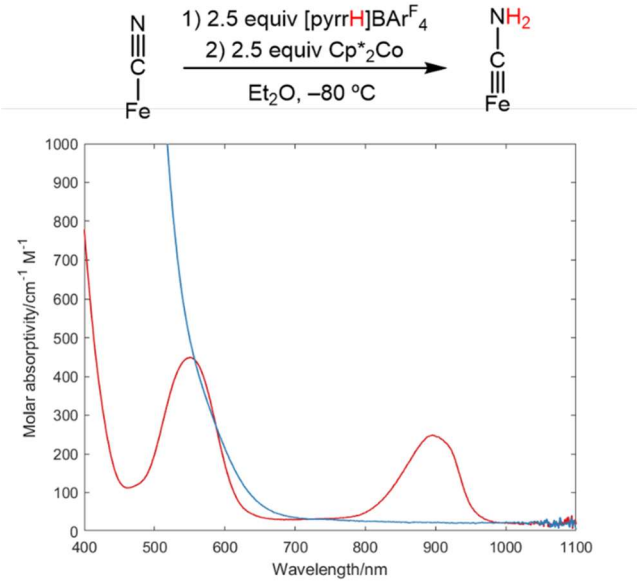

Figure B.22. UV-vis monitored addition of Cp^*_2Co (2.5 equiv per Fe) into mixture of [FeCN] (1.2 mM) and [pyrrH]BAr$^F_4$ (2.5 equiv per Fe) (Red) in Et_2O at −80°C. The final trace (Blue) shows formation of [FeCNH$_2$] and consumption of [FeCN].

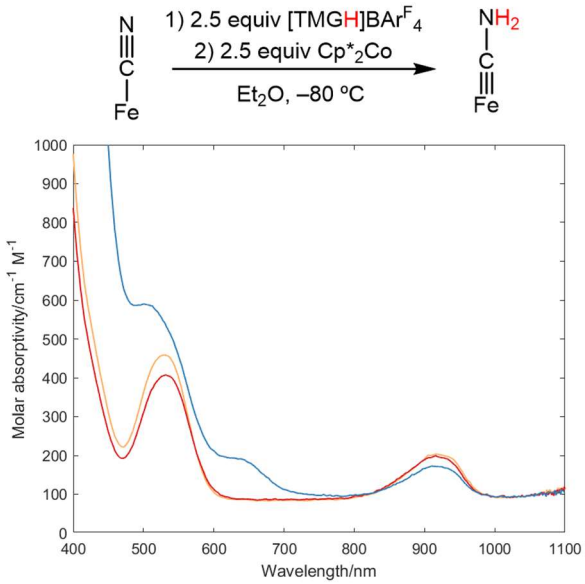

Figure B.23. UV-vis monitored addition of Cp*$_2$Co (2.5 equiv per Fe) into mixture of [FeCN] (1.2 mM) and [TMGH]BAr$^F_4$ (2.5 equiv per Fe) (Red) in Et_2O at −80°C. The final trace (Blue) shows formation of $[FeCN]^-$ and partial consumption of [FeCN]. Comparing [FeCN] before (red trace) and after addition of [TBDH]BAr$^F_4$ shows modest changes compared to those observed upon addition of [PhNH$_3$]BAr$^F_4$, suggesting only a weak interaction between [FeCN] and [TMGH]BAr$^F_4$.

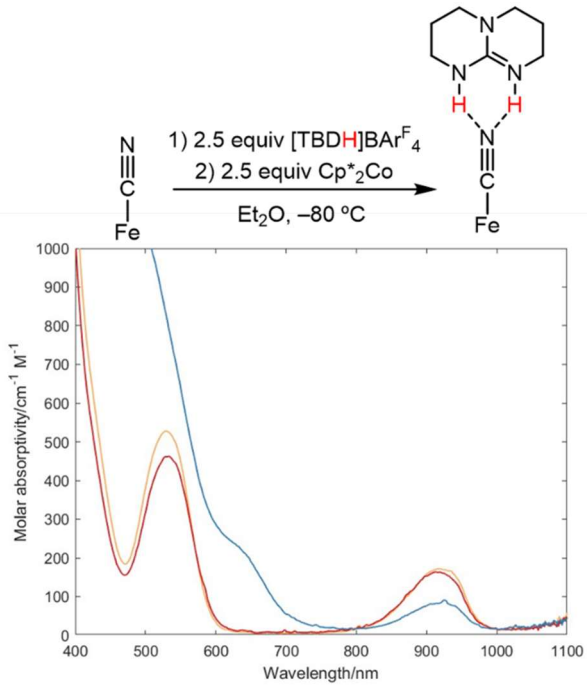

Figure B.24. UV-vis monitored addition of Cp*$_2$Co (2.5 equiv per Fe) into mixture of [FeCN] (1.2 mM) and [TBDH]BAr$^F_4$ (2.5 equiv per Fe) (Red) in Et_2O at −80°C. The final trace (Blue) shows formation of $[FeCN]^-$ and consumption of [FeCN]. Comparing [FeCN] before (red trace) and after addition of [TBDH]BAr$^F_4$ shows small changes compared to those observed upon addition of [PhNH$_3$]BAr$^F_4$, suggesting only a weak interaction between [FeCN] and [TBDH]BAr$^F_4$.

B.3.4 Additional UV-vis experiments

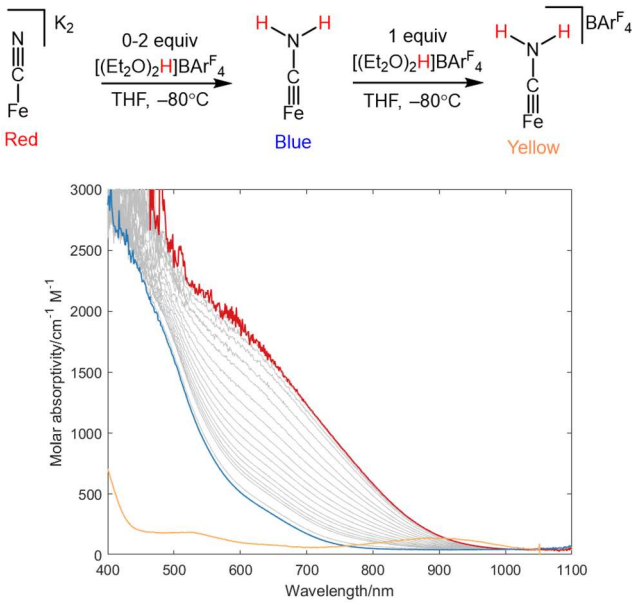

Figure B.25. UV-vis monitored addition double protonation of $[FeCN]K_2$ (red) to yield $[FeCNH_2]$ (Blue), which is similar to $[FeCNMe_2]$ with a shoulder at 620 nm and a maxima growing towards 490 nm. Addition of a third equivalent $[H(OEt_2)_2]BAr^F{}_4$ results in clean oxidation to $[FeCNH_2]BAr^F{}_4$ (yellow).

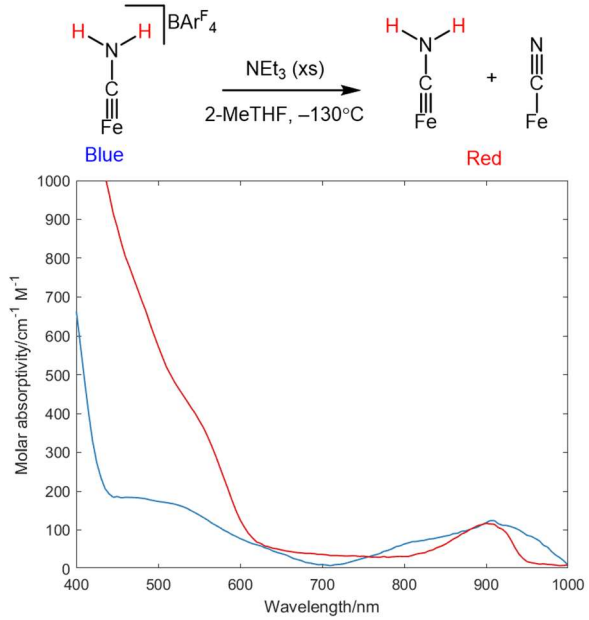

Figure B.26. UV-vis monitored deprotonation of $[FeCNH_2]BAr^F{}_4$ (Blue) by NEt_3 to yield a mixture of [FeCN] (characteristic peak at 900 nm) and $[FeCNH_2]$ (Mixture in red).

B.3.5 Measurement of equilibrium constants for H-bond formation in THF with [TBA][PF_6]

B.3.5.1 General procedure

A cuvette was loaded with [FeCN] (1 mM) in THF in 0.2 M [TBA][PF_6], sealed with a septum inside the glovebox, and then taken out of the glovebox. The system was kept air-free by an N_2 needle through the septa. Acid [HA]OTf (0 to 100 equiv) was titrated into the cuvette, with spectra recorded between titrations. The analyzed spectra were normalized to account for the decreasing concentration of [FeCN].

B.3.5.2 Data analysis

The differences between the UV-vis spectra of the H-bonded and non-H-bonded species are subtle, limiting the possibility of measuring the equilibrium constant at a single wavelength. Accordingly, we used a multivariate approach to analyzing the data and extracting equilibrium constants.[9] The following methodology was implemented in Matlab™.

For a set of collected data of titrations at varying acid concentration, the data can be presented as a matrix **Y** (dimensions: (wavelengths) x (acid concentrations)). Defining a matrix **A** as the absorbance spectra of j number of species in solution (dimensions: (wavelengths) x (j concentrations) and a matrix **C** as the concentration of j species with varying acid concentration (dimensions: (j) x (acid concentrations)) we define an equation:

$$\mathbf{Y} = \mathbf{AC} + \mathbf{R} \quad \text{(eqn B.6)}$$

where **R** is the residual.

Building a model around the equilibrium:

$$[\text{FeCN}][\text{HA(OTf)}] = K[\text{FeCN}\cdots\text{HA(OTf)}] \quad \text{(eqn B.7)}$$

We can readily calculate the matrix $\mathbf{C}(K)$ for a given equilibrium constant. Seeking to minimize $\mathbf{R^2}$ for a given K we can calculate the absorbance spectra $\mathbf{A'}(K)$ using equation eqn B.8.

$$\mathbf{A'}(K) = \mathbf{Y}(\mathbf{C}(K)^{+}) \quad \text{(eqn B.8)}$$

Where $\mathbf{C}^{+}(K)$ is the pseudo-inverse of $\mathbf{C}(K)$.

This allows us to define **R** as a function of K

$$\mathbf{R}(K) = \mathbf{A'}(K)\mathbf{C}(K) \quad \text{(eqn B.9)}$$

which the square $\mathbf{R^2}$ can be minimized against K.

To analyze the model's predicted absorbances of [FeCN] and [FeCN···HA(OTf)] are printed along with the residuals. In addition, the absorbance at 563 nm and 880 nm, areas with larger divergence, were used to estimate the concentration of [FeCN] and [FeCN···HA(OTf)] and compared to the calculated concentration. The error bars were determined by testing varying sizes of K to see when the predicted absorbances±error bar could capture ~70% of the measured absorbances.

B.3.5.3 Titration experiments

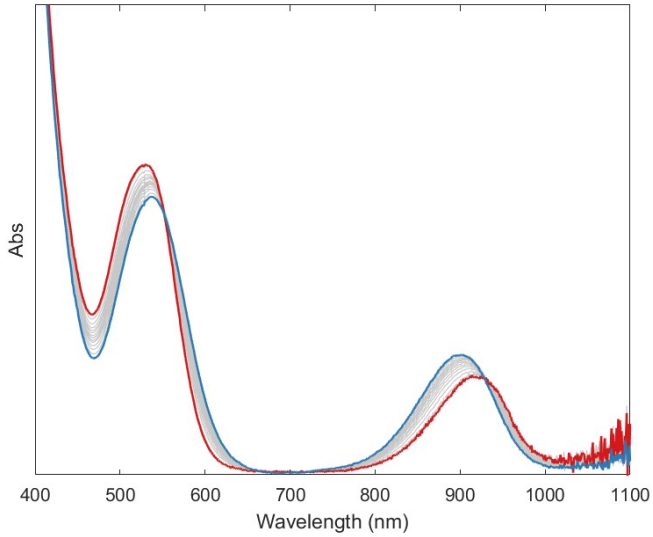

Figure B.27. UV-vis monitored titration of [$PhNH_3$]OTf (0 to 100 mM) into [FeCN] 1 mM in THF with 0.2 M [TBA][PF_6] at 25 °C.

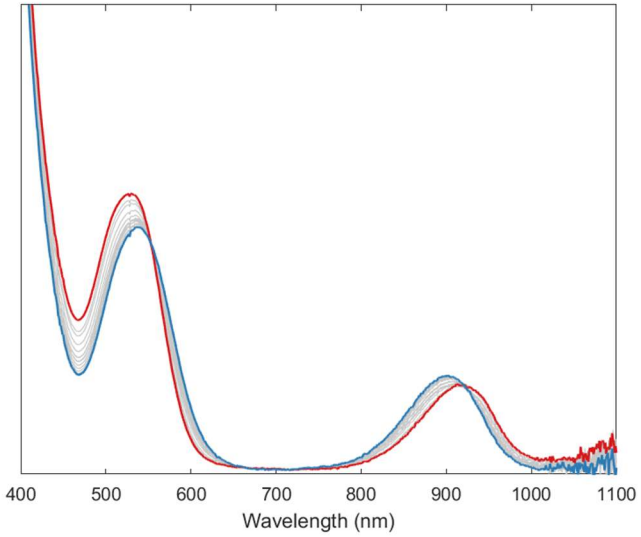

Figure B.28. UV-vis monitored titration of [$^{4\text{-Cl-2,6-Me}}$pyH]OTf (0 to 100 mM) into [FeCN] 1 mM in THF with 0.2 M [TBA][PF_6] at 25 °C.

B.3.5.4 Outputs from Multivariate Fitting Model

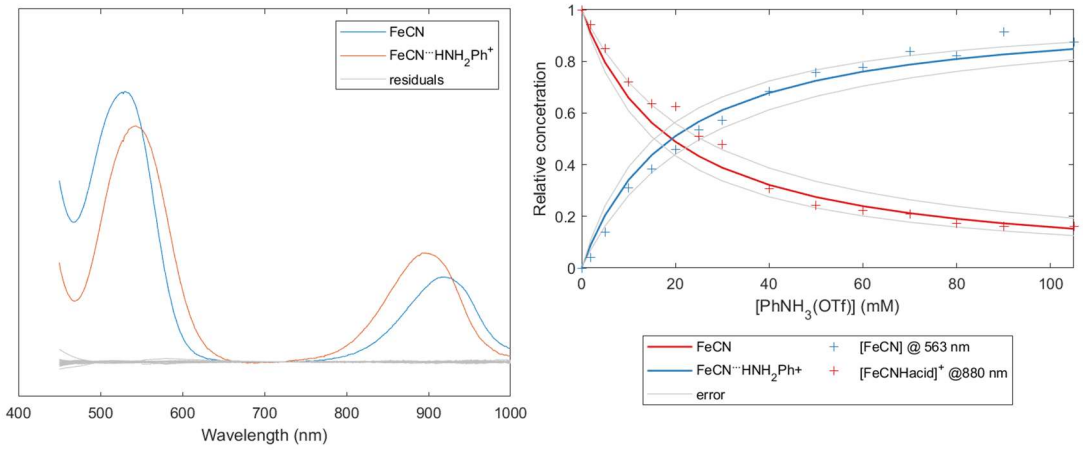

Figure B.29. Predicted spectra (left) of [FeCN] and [FeCN···HNH_2Ph(OTf)] with residual spectra shown in grey. Calculated solid lines (red) were compared to those implied by absorbances (right), with error bars indicated. An equilibrium constant of K = 62 ±15 M^{-1} was determined.

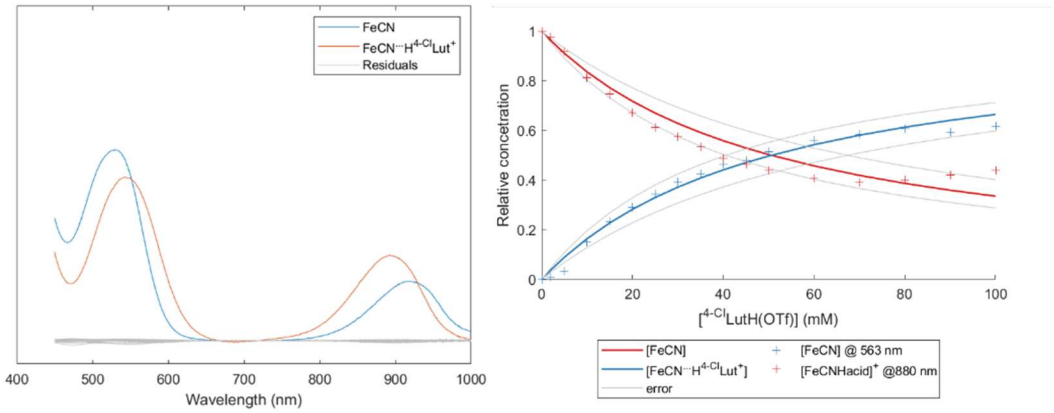

Figure B.30. Predicted spectra (left) of [FeCN] and [FeCN···H(4-Cl-2,6-mepyr)(OTf)] with residual spectra shown in grey. Calculated solid lines (red) were compared to those implied by absorbances (right), with error bars indicated. An equilibrium constant of $K = 20 \pm 5$ M^{-1} was determined.

B.4 Kinetic studies

B.4.1 General procedure

Kinetic analysis was performed by UV-vis, using the Cary *ScanningKinetics* program to record UV-vis traces (every 6 seconds). A cuvette was loaded with [FeCN] and $[PhNH_3]BAr^F{}_4$ in 4:1 2MeTHF:THF, sealed with a septa in the glovebox. It was then taken out and loaded into a UNISOKO cooling apparatus connected to the UV-vis. The cuvette was then cooled to −145°C and allowed to equilibrate for at least 20 minutes. Spectra were typically collected every minute while equilibrating to ensure no icing on the cuvette and sufficient stirring. The system was kept air-free by an N_2 needle through the septa.

After equilibration, the reductant was added via syringe. A thick syringe (18 gauge) was found to be most suitable, as the greater force of addition allowed for faster mixing of the solution. Similarly, the needle had to be long enough to be submerged in the ethereal solution, such that the reductant was added directly into the solution, not on top of the liquid. With these precautions, mixing was fast enough (<10 s) that kinetic analysis was possible, monitoring the decay of [FeCN] by loss of the characteristic peak at 895 nm. The kinetic values are summarized in **Table B.3**. Plots of Abs_{895} vs. t and log(A895) vs. t are supplied in Figure **B.32-B.47**. It was found that the data generally fit a 1st order plot, not a 2nd order plot (**Figure B.31**).

The error was analyzed for the kobs and k2nd derived for each individual kinetic run (**Table B.3**). The mean error for each run (±0.06 M^{-1} s^{-1} for k_{2nd}) closely resembles the spread in values for the straight-line plot used to derive k_{2nd} (±0.07 M^{-1} s^{-1}).

Table B.3. Summary of kinetics data with slope and associated rate constants derived from slope.

	Concentrations (mM)			Ratio to [FeCN]					
Run	**FeCN**	**$[PhNH_3]BAr^F_4$**	**$^{Et}Cp_2Co$**	**$[PhNH_3]BAr^F_4$**	**$^{Et}Cp_2Co$**	**Slope**	**k_{obs} (s^{-1})**	**k_{2nd} (M^{-1} s^{-1})**	**Notes**
A	1.2	3.7	19.4	3	16	-1.35±0.09	2.25±0.15 ·10^{-2}	1.16±0.08	Varying reductant
B	1.2	3.5	43.0	3	37	-3.0±0.2	5.0±0.4·10^{-2}	1.17±0.09	"
C	1.2	3.5	33.1	3	28	-2.19±0.08	3.66±0.13·10^{-2}	1.11±0.04	"
D	1.1	3.4	47.7	3	42	-3.3±0.2	5.5±0.3·10^{-2}	1.16±0.07	"
E	1.2	3.6	24.4	3	20	-1.5±0.25	2.5±0.4·10^{-2}	1.02±0.17	"
F	1.2	3.5	35.2	3	30	-2.52±0.09	4.21±0.15·10^{-2}	1.19±0.04	"
G	1.2	3.6	31.1	3	26	-1.88±0.06	3.13±0.10·10^{-2}	1.01±0.03	"
								1.17±0.07	k_{2nd} averaged
H	2.1	6.4	29.9	3	14	-2.06±0.06	3.44±0.10·10^{-2}	1.15±0.03	Varying [FeCN]
I	1.7	5.1	26.5	3	16	-1.75±0.09	2.91±0.15·10^{-2}	1.10±0.06	"
J	1.4	4.3	37.1	3	26	-3.0±0.4	5.0±0.7·10^{-2}	1.34±0.19	"
K	1.2	7.0	38.1	6	33	-3.1±0.14	5.2±0.2·10^{-2}	1.36±0.06	Varying acid
L	1.1	10.1	20.9	9	19	-1.54±0.07	2.57±0.12·10^{-2}	1.23±0.06	"
M	1.1	13.3	25.8	12	23	-1.8±0.10	3.0±0.2·10^{-2}	1.16±0.07	"
N	1.1	13.5	20.9	12	19	-1.64±0.07	2.73±0.11·10^{-2}	1.31±0.05	"
O(D)	1.2	3.5	33.1	3	28	-1.72±0.06	2.86±0.09·10^{-2}	0.86±0.03	Deuterated acid
P(D)	1.2	3.5	33.1	3	28	-1.66±0.04	2.76±0.06·10^{-2}	0.83±0.02	Deuterated acid
								0.85±0.02	k_{2nd} averaged, deuterated
							KIE	1.37±0.06	

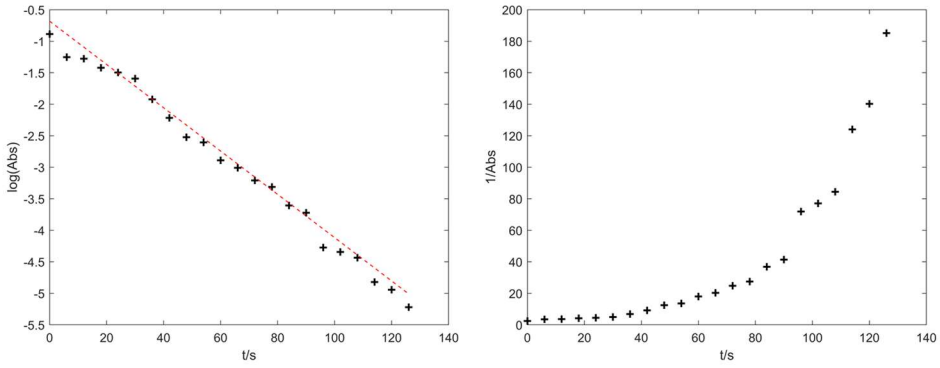

Figure B.31. Plots of log(abs) vs. t (1st order) and 1/Abs vs. t (2nd order) of [FeCN] decay after the addition of reductant. Straight-line is only observed for 1st order plot, suggesting a reaction first order in [FeCN]. This was confirmed (Figure 3.8D, runs H-J), where no difference was found in the k_{2nd} when varying [FeCN].

B.4.2 First-order plots for individual runs

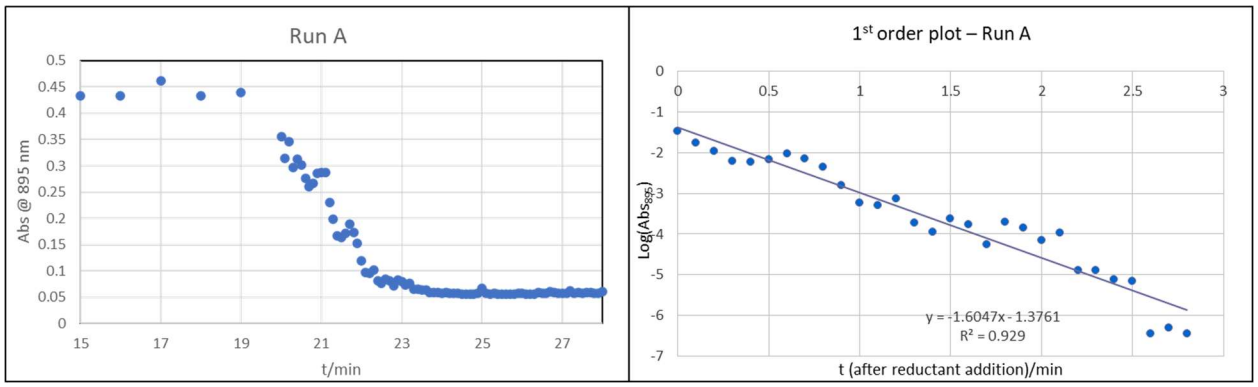

Figure B.32. Trace of Abs_{895} vs. t (left) and log(Abs895) vs. t plot (right) for run A.

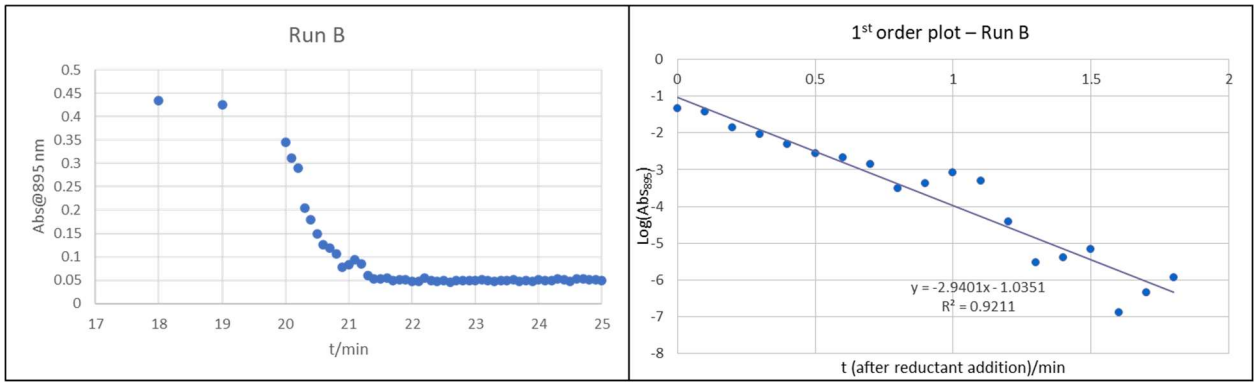

Figure B.33. Trace of Abs_{895} vs. t (left) and log(Abs895) vs. t plot (right) for run B.

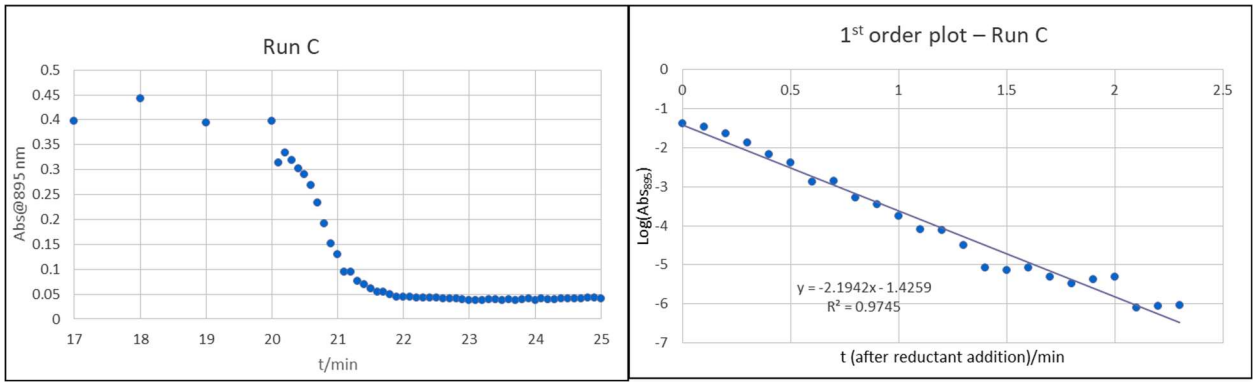

Figure B.34. Trace of Abs_{895} vs. t (left) and log(Abs895) vs. t plot (right) for run C.

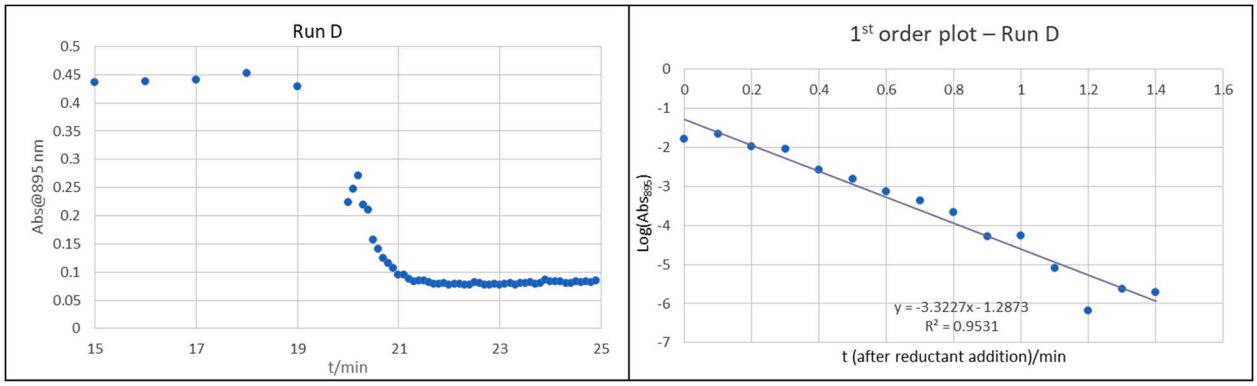

Figure B.35. Trace of Abs_{895} vs. t (left) and log(Abs895) vs. t plot (right) for run D.

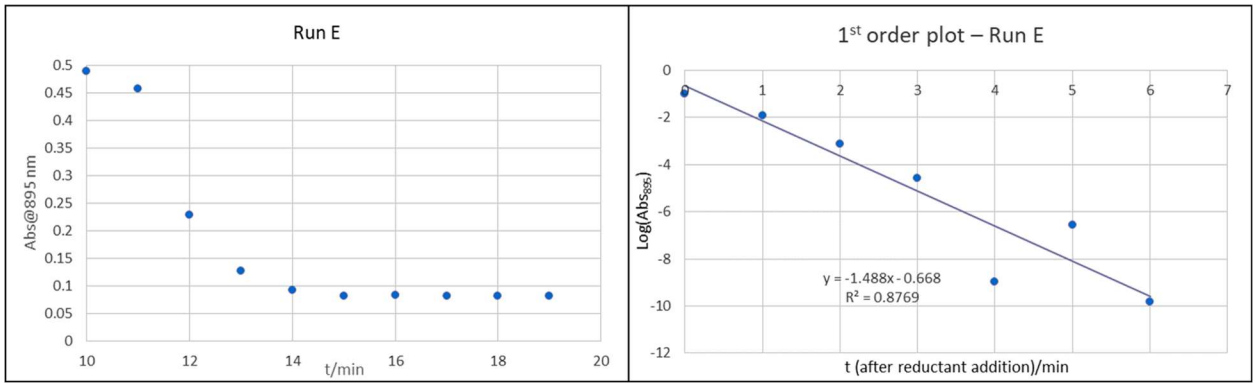

Figure B.36. Trace of Abs_{895} vs. t (left) and log(Abs895) vs. t plot (right) for run E.

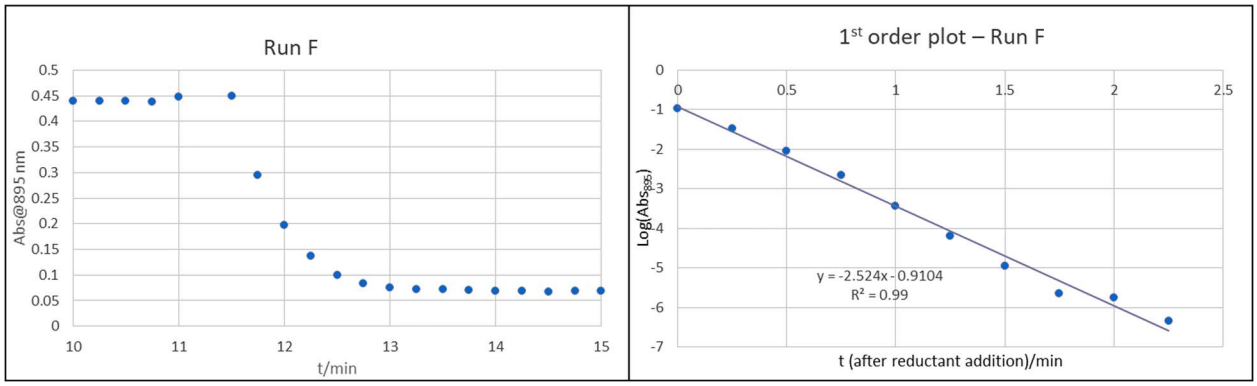

Figure B.37. Trace of Abs_{895} vs. t (left) and log(Abs895) vs. t plot (right) for run F.

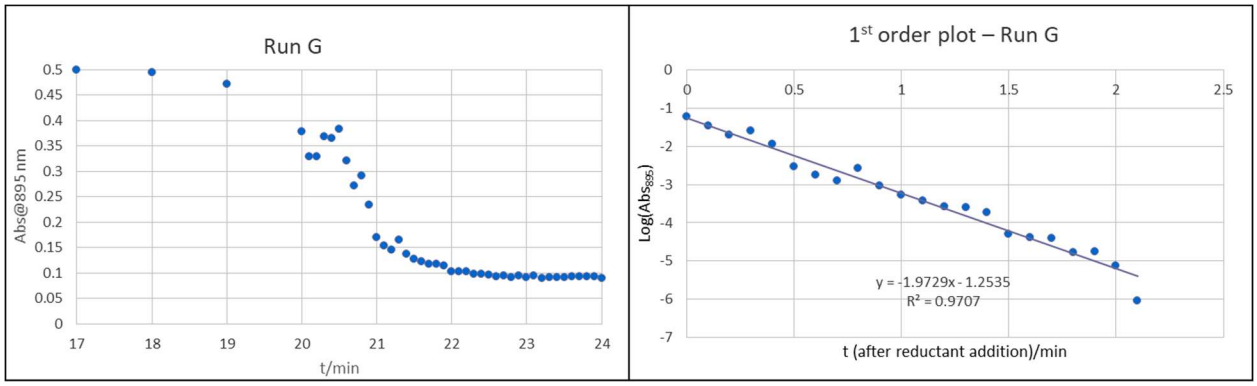

Figure B.38. Trace of Abs_{895} vs. t (left) and log(Abs895) vs. t plot (right) for run G.

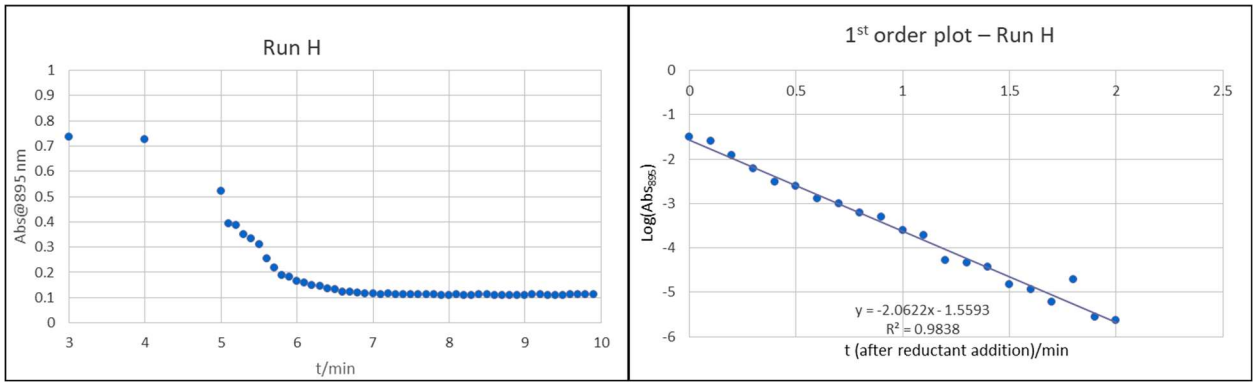

Figure B.39. Trace of Abs_{895} vs. t (left) and log(Abs895) vs. t plot (right) for run H.

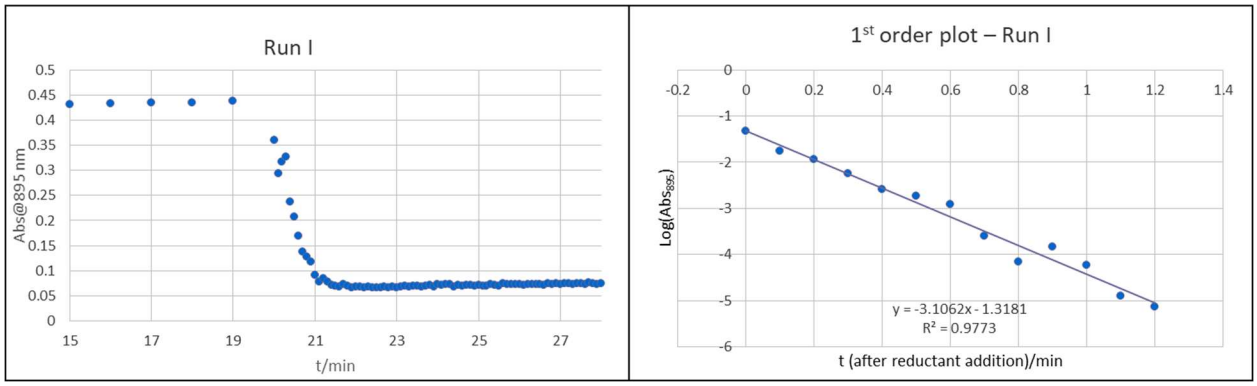

Figure B.40. Trace of Abs_{895} vs. t (left) and log(Abs895) vs. t plot (right) for run I.

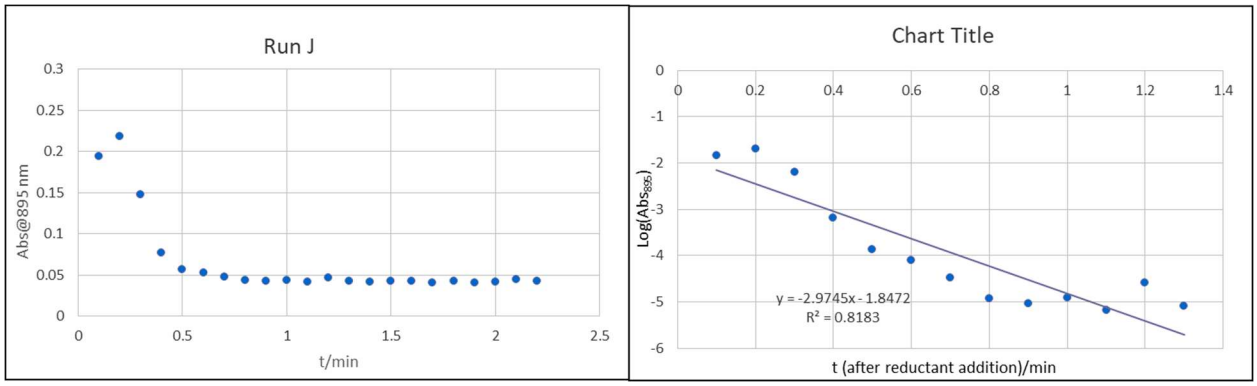

Figure B.41. Trace of Abs_{895} vs. t (left) and log(Abs895) vs. t plot (right) for run J.

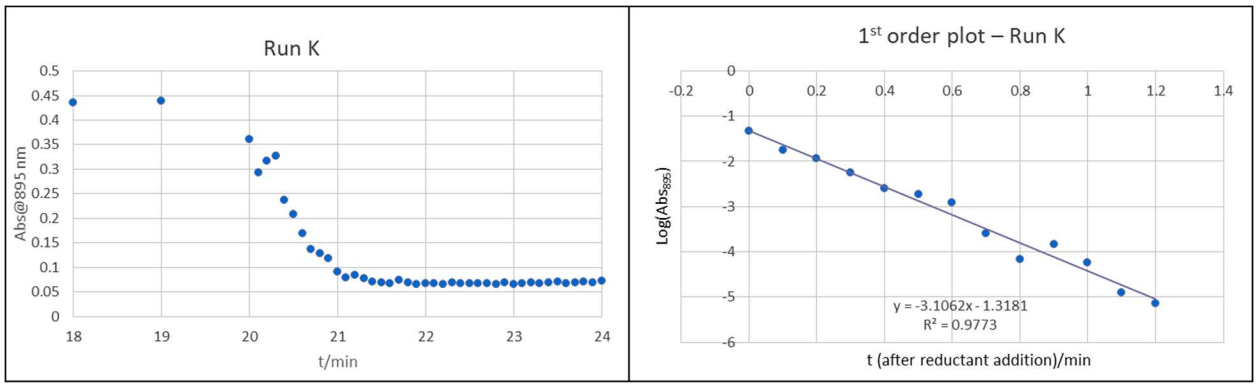

Figure B.42. Trace of Abs_{895} vs. t (left) and log(Abs895) vs. t plot (right) for run K.

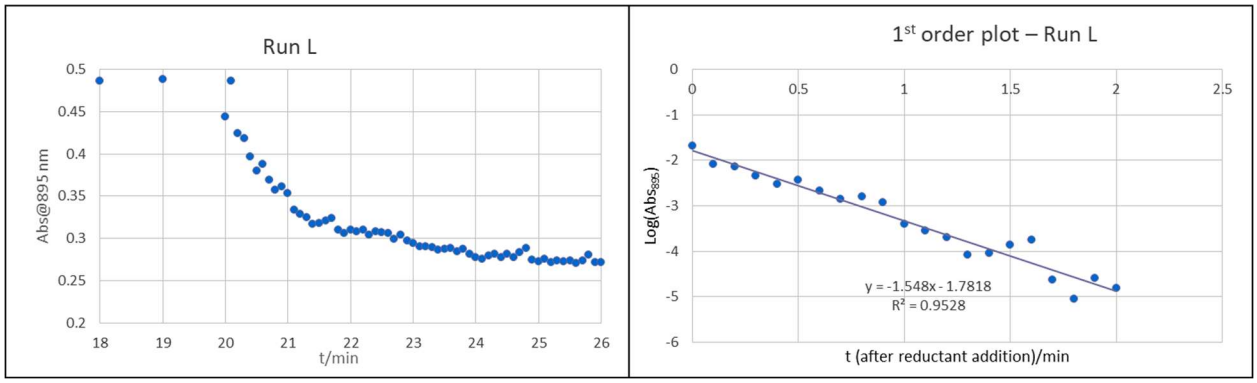

Figure B.43. Trace of Abs_{895} vs. t (left) and log(Abs895) vs. t plot (right) for run L.

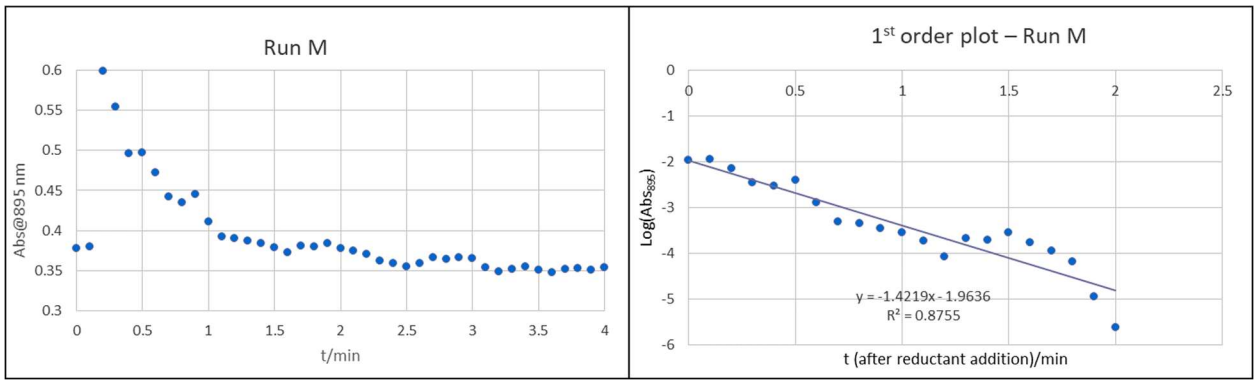

Figure B.44. Trace of Abs_{895} vs. t (left) and log(Abs895) vs. t plot (right) for run M.

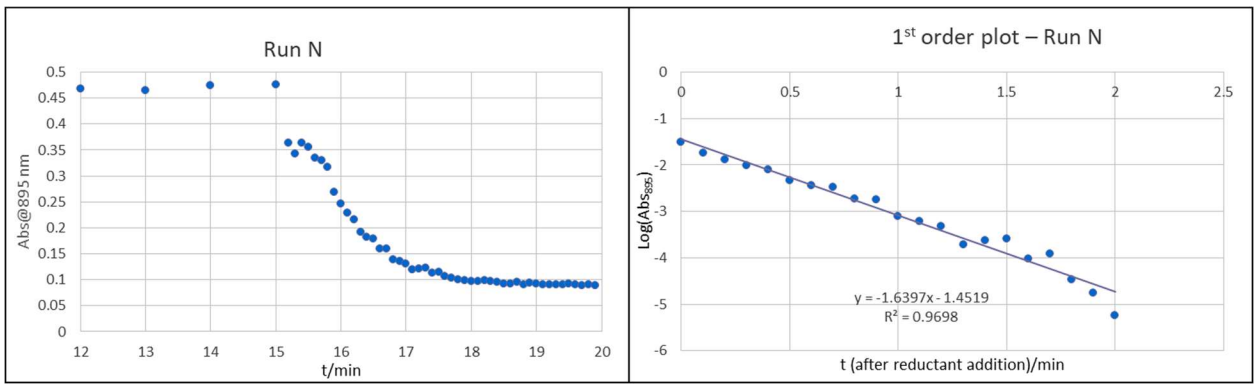

Figure B.45. Trace of Abs_{895} vs. t (left) and log(Abs895) vs. t plot (right) for run N.

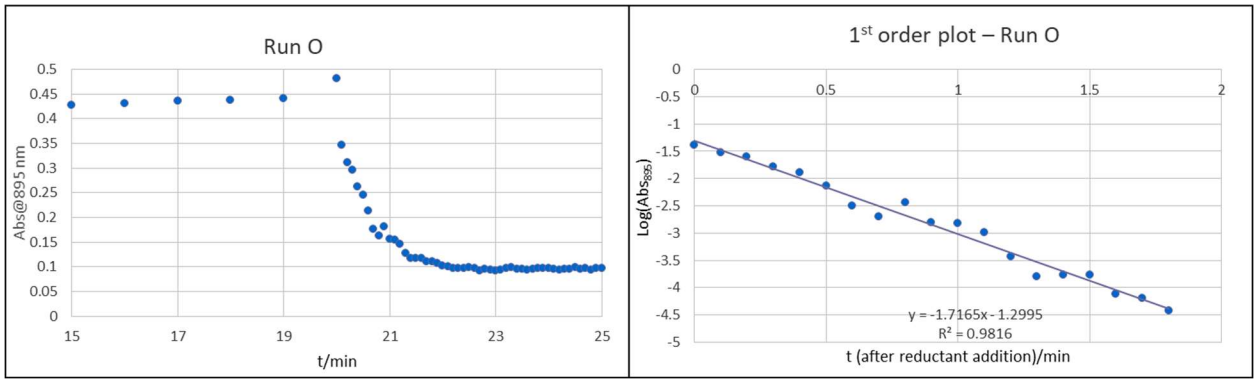

Figure B.46. Trace of Abs_{895} vs. t (left) and log(Abs895) vs. t plot (right) for run O.

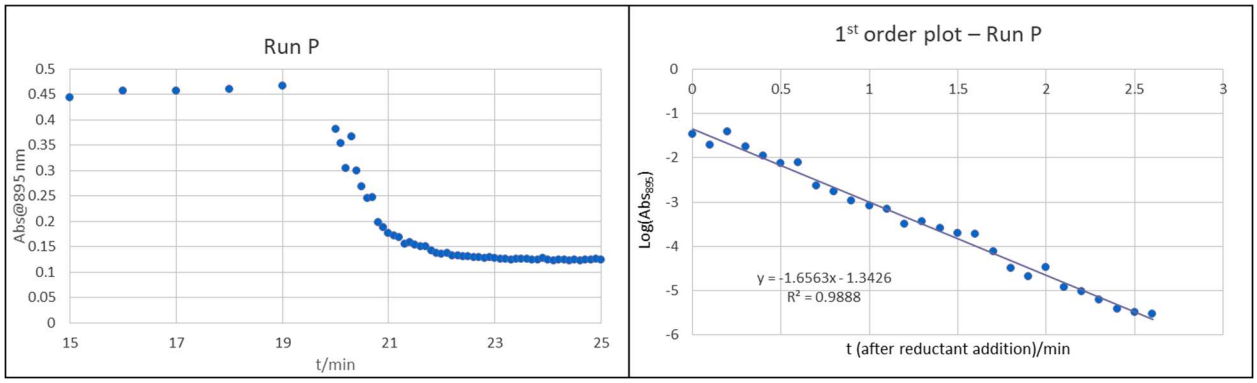

Figure B.47. Trace of Abs_{895} vs. t (left) and log(Abs895) vs. t plot (right) for run P.

B.5 ^{57}Fe Mössbauer spectroscopy

B.5.1 Note on the fitting of Mössbauer spectra

Data analysis was performed using version 4 of the program WMOSS (www.wmoss.org) and quadrupole doublets were fit to Lorentzian lineshapes. Simulations were constructed from the minimum number of quadrupole doublets required to attain a quality fit to the data (convergence of χ_R^2). Quadrupole doublets were constrained to be symmetric. Using the non-linear error analysis algorithm provided by WMOSS, the errors in the computed parameters are estimated to be 0.02 mm s^{-1} for δ and 2% for ΔE_Q.

B.5.2 Freeze-Quenched Mössbauer spectroscopy of reduction reactions

General Procedure for Freeze-Quench Mössbauer Spectroscopy of reactions. All solvents are stirred with Na/K for ≥ 2 hours and filtered prior to use. In a nitrogen filled

glovebox, the desired ^{57}Fe species (0.0023 mmol) is dissolved in 0.3 mL Et_2O and cooled to -78 °C in a stirring vial in the glovebox cold well. Acid was added in 0.1 mL Et_2O. Reductant was added in 0.3 mL to the chilled vial. The reaction was allowed to stir for 5 minutes before it was rapidly transferred to a pre-chilled Mössbauer cup. The cold well was then changed from -78°C (195 K) to 77 K and the solution froze within 5 minutes. The Mössbauer cup was kept at 77 K for minimum 20 minutes before being rapidly taken out of the glovebox and submerged in liquid N_2 before being mounted on the Mössbauer spectrometer.

B.5.3 Freeze-Quenched ^{57}Fe Mössbauer spectra of individual reactions

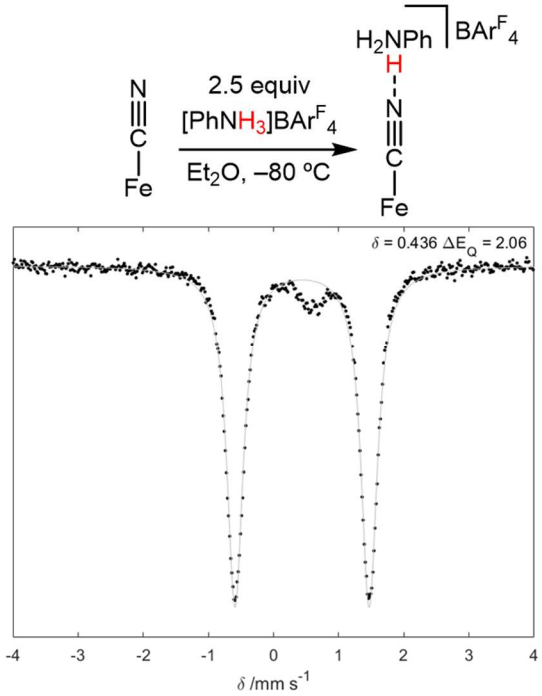

Figure B.48. Freeze-quenched Mössbauer of reaction of [FeCN] with $[PhNH_3]BAr^F{}_4$.

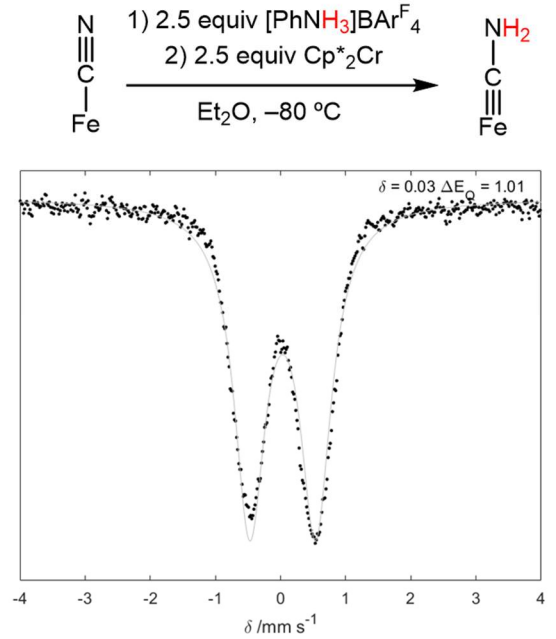

Figure B.49. Freeze-quenched Mössbauer of reaction of [FeCN] with $[PhNH_3]BAr^F{}_4$ and $Cp^*{}_2Cr$.

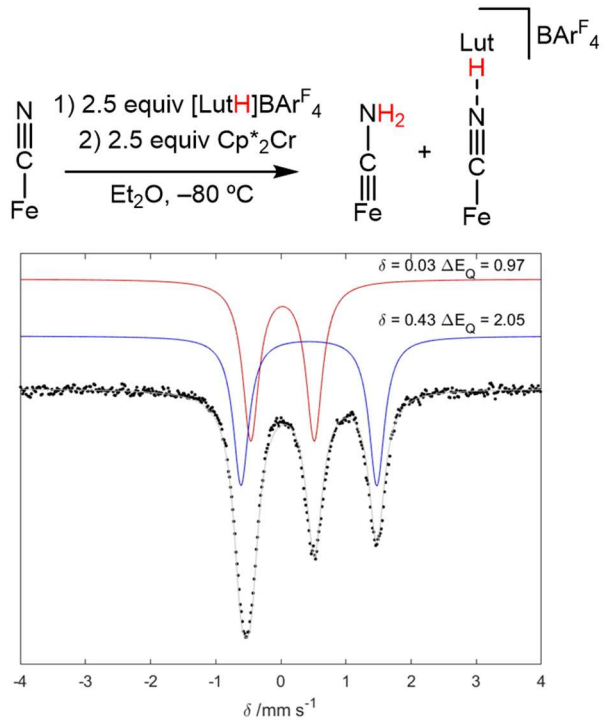

Figure B.50. Freeze-quenched Mössbauer of reaction of [FeCN] with $[LutH]BAr^F{}_4$ and $Cp^*{}_2Cr$.

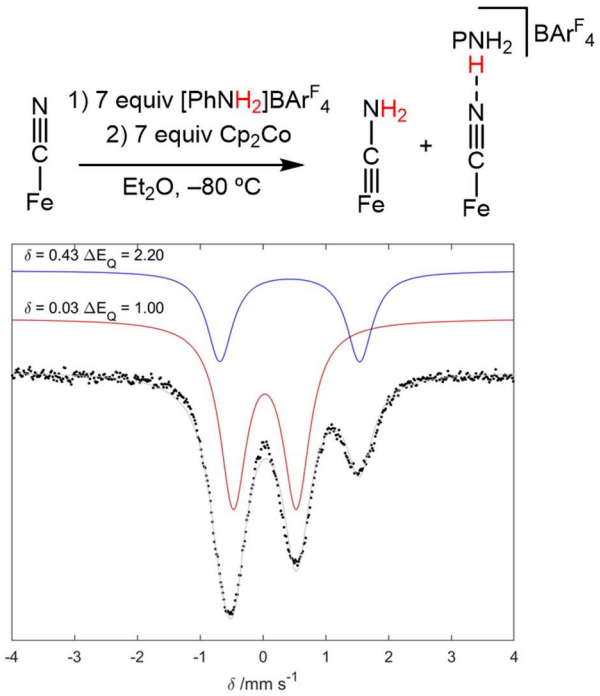

Figure B.51. Freeze-quenched Mössbauer of reaction of [FeCN] with $[PhNH_2]BAr^F{}_4$ and $Cp^*{}_2Cr$.

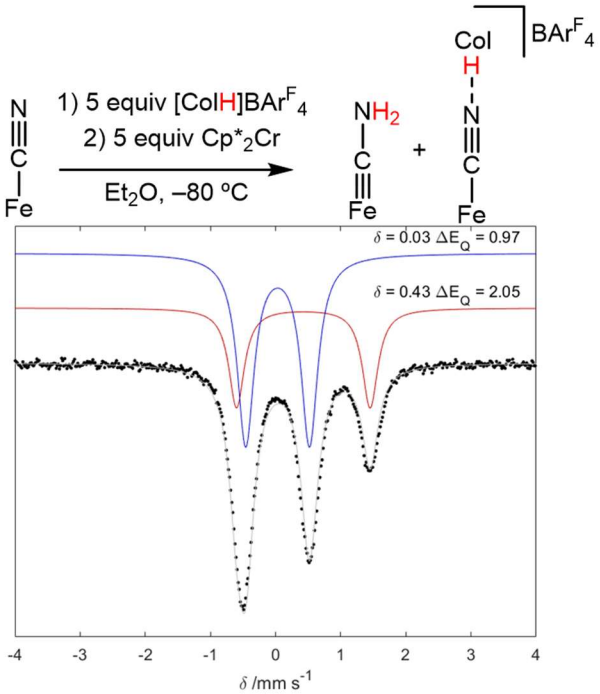

Figure B.52. Freeze-quenched Mössbauer of reaction of [FeCN] with $[ColH]BAr^F{}_4$ and $Cp^*{}_2Cr$.

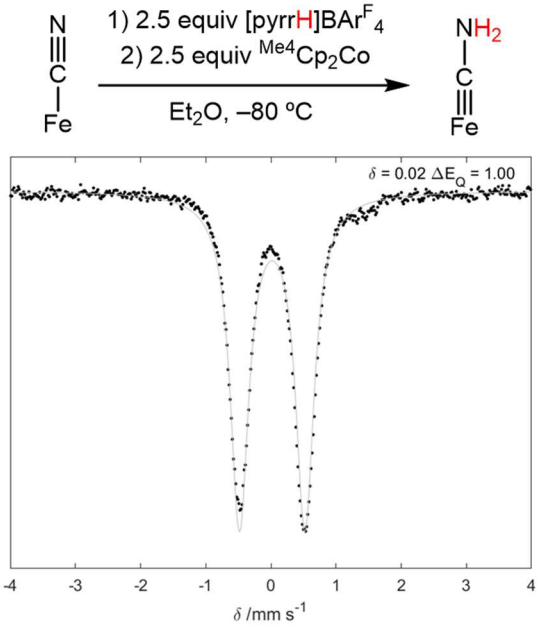

Figure B.53. Freeze-quenched Mössbauer of reaction of [FeCN] with [pyrrH]BAr$^F_4$ and $^{Me4}Cp_2Co$.

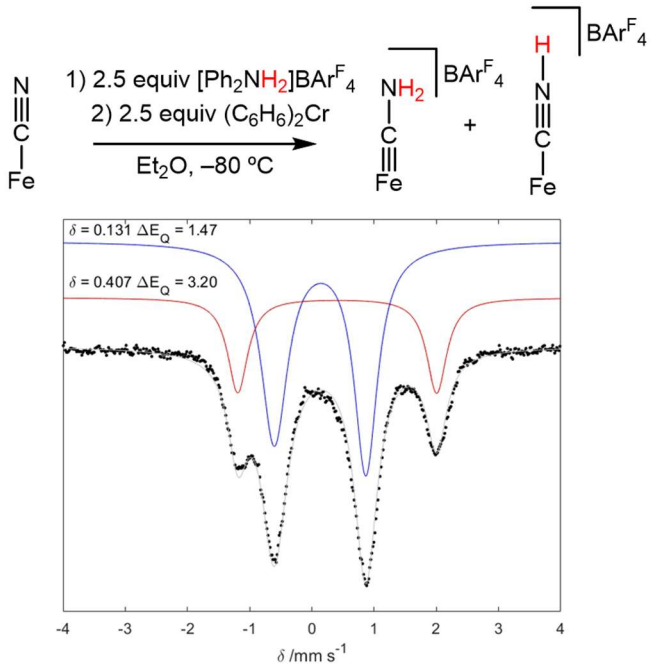

Figure B.54. Freeze-quenched Mössbauer of reaction of [FeCN] with [Ph$_2$NH$_2$]BAr$^F_4$ and Cp_2Co.

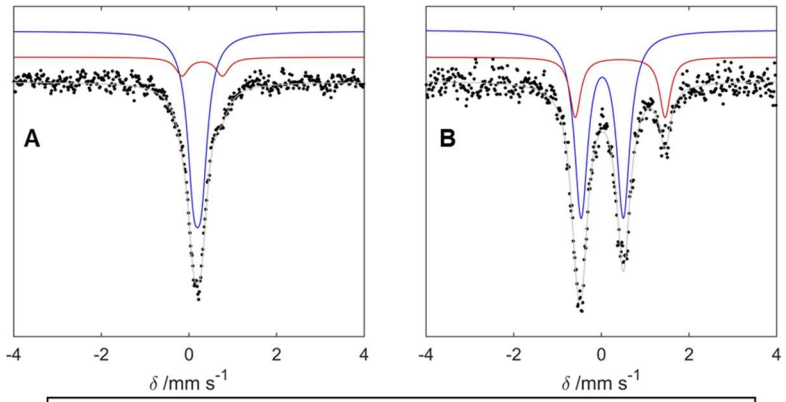

^{57}Fe spectra A			
δ(mm s^{-1})	ΔE_Q (mm s^{-1})	Γ (mm s^{-1})	Rel. area
0.20±0.01	0.18±0.05	0.35±0.05	86% (Blue)
0.30±0.01	0.92±0.05	0.36±0.03	14% (Red)

^{57}Fe spectra B			
δ(mm s^{-1})	ΔE_Q (mm s^{-1})	Γ (mm s^{-1})	Rel. area
0.02±0.01	0.96±0.01	0.37±0.01	80% (Blue)
0.43±0.01	2.09±0.01	0.30±0.01	20% (Red)

Figure B.55. Mössbauer spectrum of reaction of P_3^{Si}FeCN with sequentially KC_8 (excess), spectra A and 2 equiv $[H(OEt_2)_2]BAr^F{}_4$.

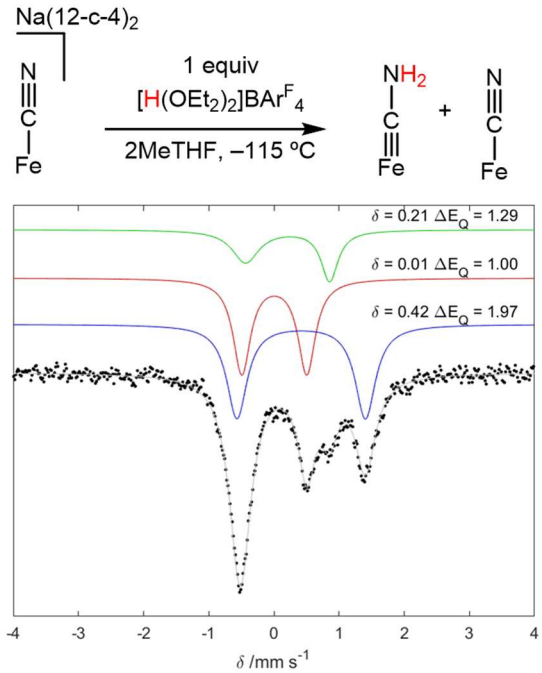

Figure B.56. Freeze-quenched Mössbauer of reaction of [FeCN][Na(12-c-4)$_2$] with $[H(OEt_2)_2]BAr^F{}_4$.

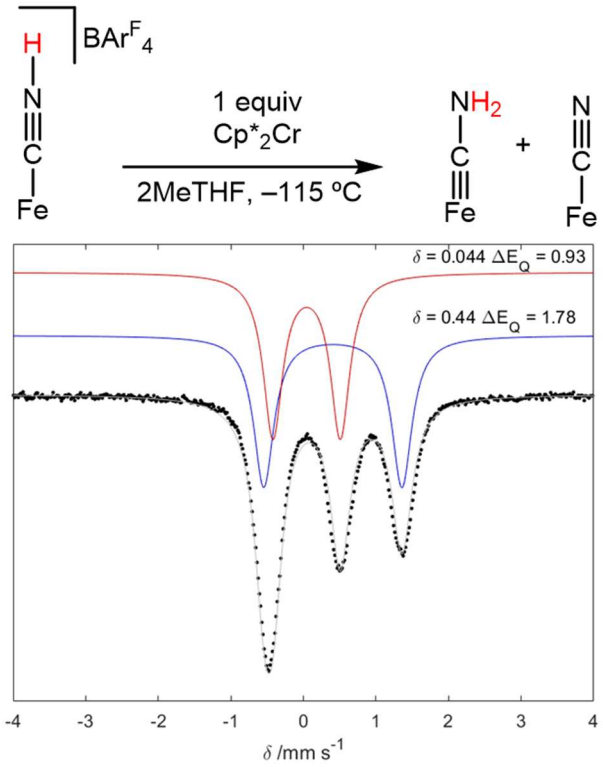

Figure B.57. Freeze-quenched Mössbauer of reaction of [FeCNH]BAr$^F_4$ with Cp*$_2$Cr.

B.6 IR spectroscopy

B.6.1 Solution state IR measurement of [FeCN···HNH$_2$Ph]BAr$^F_4$

B.6.1.1 General procedure

Inside the dry box a 5 mM solution of [FeCN] in 2-MeTHF 1 mL, was loaded into an IR-cell with KBr-windows and cooled to −78°C in the cold-well. After equilibration (15 minutes), the cell was rapidly removed from the cold-well and placed in an IR holder, allowing the beam to transport to the cell. After collection, the same procedure was followed, but 2.5 equiv [PhNH$_3$]BAr$^F_4$ (12.5 mM) was added.

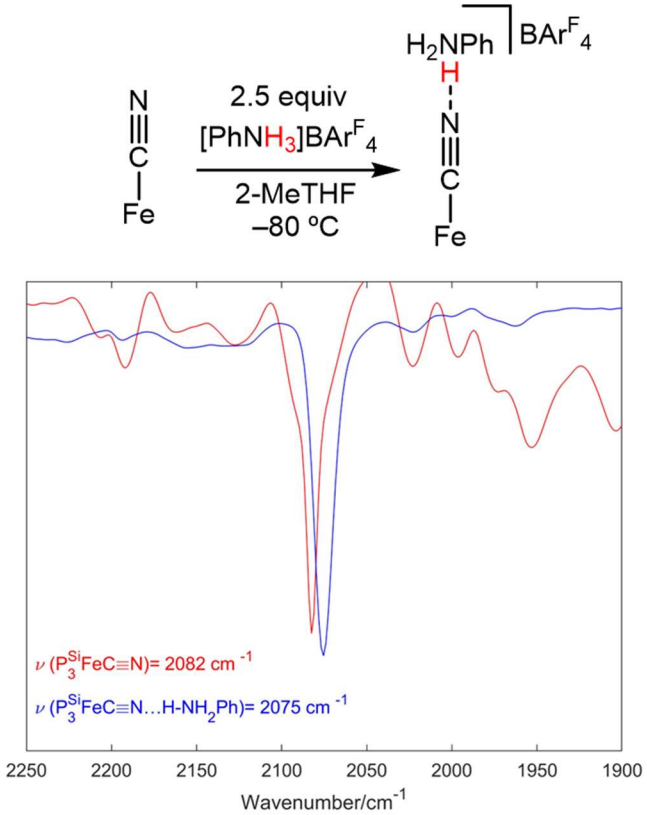

Figure B.58. IR comparison of [FeCN] with and without 2.5 equiv $[PhNH_2]OTf$ added. The weak shift of ν_{CN} suggests weak activation of [FeCN] consistent with an H-bond.

B.6.2 Solid state IR measurement of [FeCN···HTBD]

B.6.2.1 General procedure

Inside the dry box a, 10 mM solution of $[FeCN][Na(12\text{-}c\text{-}4)_2]$ (5 mg, 4.7 μmol) in 0.5 mL Et_2O was cooled to −78°C. $[TBDH]BAr^F_4$ (4.7 mg, 1 equiv) was added, and the reaction was allowed to stir for 5 minutes. 10 mL benzene was added slowly, such that it froze rapidly, upon addition. Subsequently, the solvent was removed in vacuo with care taken such that the benzene remained frozen, forming a lyophilized powder. This solid was then analyzed by IR, showing a slightly activated ν_{CN} = 1978 cm^{-1} compared to 2014 cm^{-1} in the $[FeCN][Na(12\text{-}c\text{-}4)_2]$ starting material. This stretch was confirmed to be from CN^- ligand by using the $[FeC^{15}N][Na(12\text{-}c\text{-}4)_2]$; the resulting ν_{C15N} = 1944 cm^{-1} is consistent with isotopic labeling (1947 cm^{-1} assuming harmonic oscillator model).

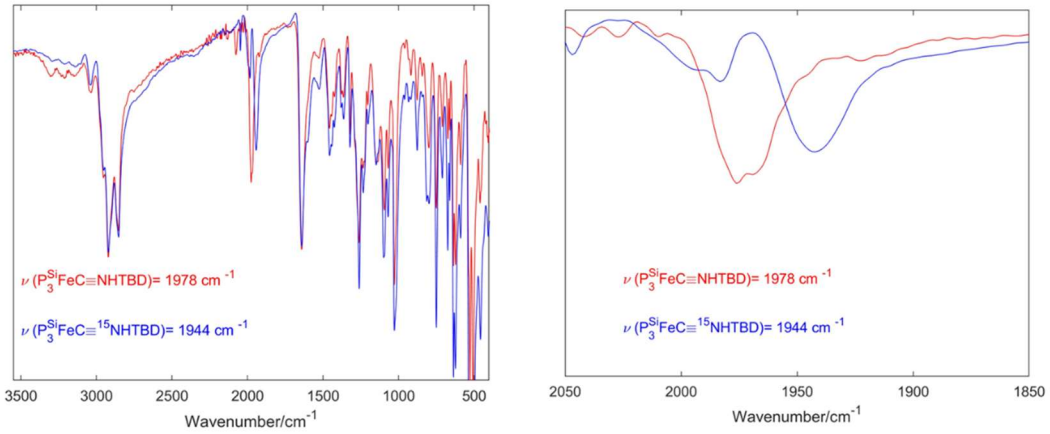

Figure B.59. Solid state IR of [FeCN···HTBD] and [FeC^{15}N···HTBD].

B.7 EPR spectroscopy

B.7.1 Generation of cw-EPR samples

The reaction of [FeCN] with weak acid ([TMGH]BAr$^{F}_{4}$ or [TBDH]BAr$^{F}_{4}$) and Cp*$_2$Co was monitored by cw-EPR. A 0.5 mL solution of [FeCN] (4 mM) in 2-MeTHF was cooled to −78°C, and acid (5 equiv) and reductant (5 equiv) were added as solids. The solution was allowed to stir for 5 minutes, then rapidly transferred to a X-band EPR tube, frozen at 77 K, and then analyzed.

Samples of [FeCN][Na(12-c-4)$_2$] + [TBD]OTf and [FeCN] with Cp*$_2$Co were prepared analogously, but only acid or reductant was added.

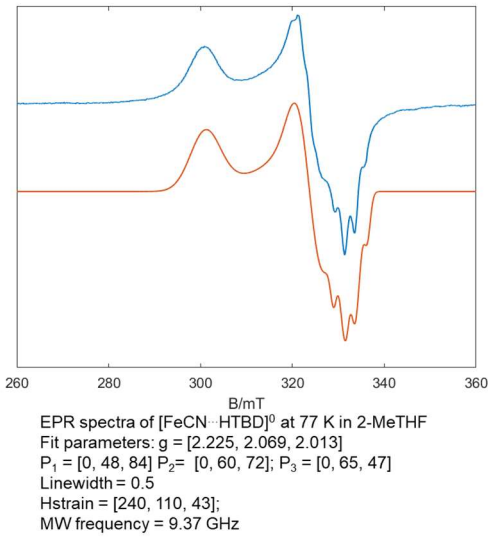

Figure B.60. X-band EPR spectra of independently synthesized $[Fe^{I}CN\cdots HTBD]^{0}$ (blue trace), collected at 2 mM concentration in 2-MeTHF at 77 K with fit (orange trace).

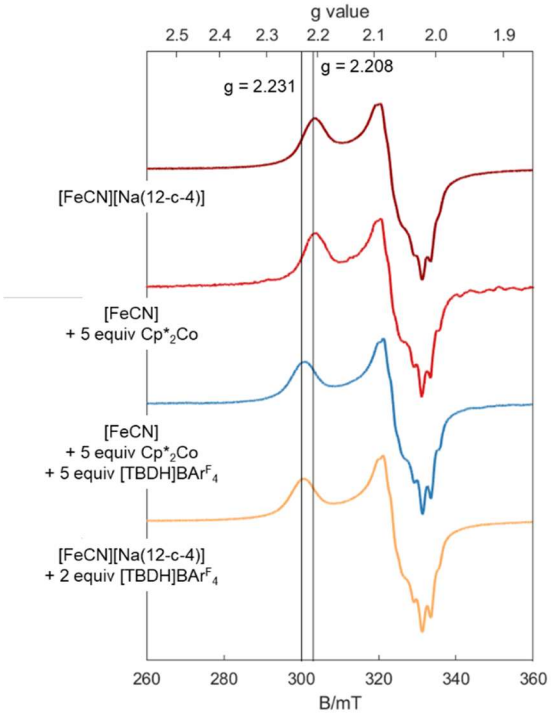

Figure B.61. X-band EPR spectra of compounds and reactions listed, collected at 2 mM concentration in 2-MeTHF at 77 K. Lines at g = 2.31 and 2.208 used to highlight shift in $g_{\parallel}$ between H-bonded and non H-bonded $[Fe^{I}CN]^{-}$ species.

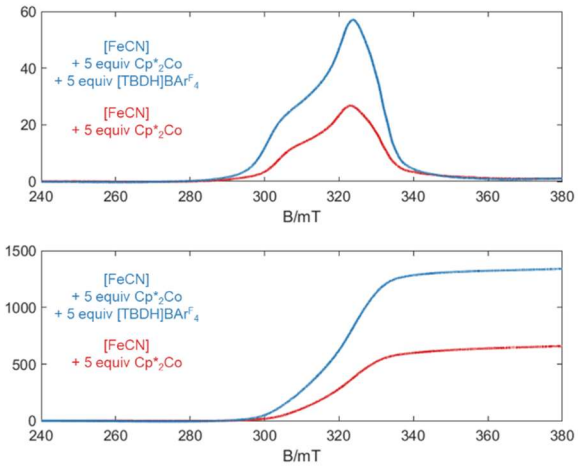

Figure B.62. Integral (top) and double integral (bottom) of X-band EPR spectra of compounds and reactions listed, collected at 2 mM concentration in 2-MeTHF at 77 K. Double integral shows that reaction with [TBDH]BAr^F_4 accounts for ~ double the intensity of the reaction without acid.

B.8 Electrochemical methods

B.8.1 General procedure

Electrochemical measurements were conducted with a glassy carbon working electrode, a platinum wire counter electrode, and an Ag/AgOTf reference electrode isolated by a CoralPor™ frit (obtained from BASi) and referenced externally to $Fc^{+/0}$. Unless specified, NaK-dried THF was used as a solvent, with 0.2 M [TBA][PF_6] electrolyte. Measurements conducted with a CH Instruments 600B electrochemical analyzer.

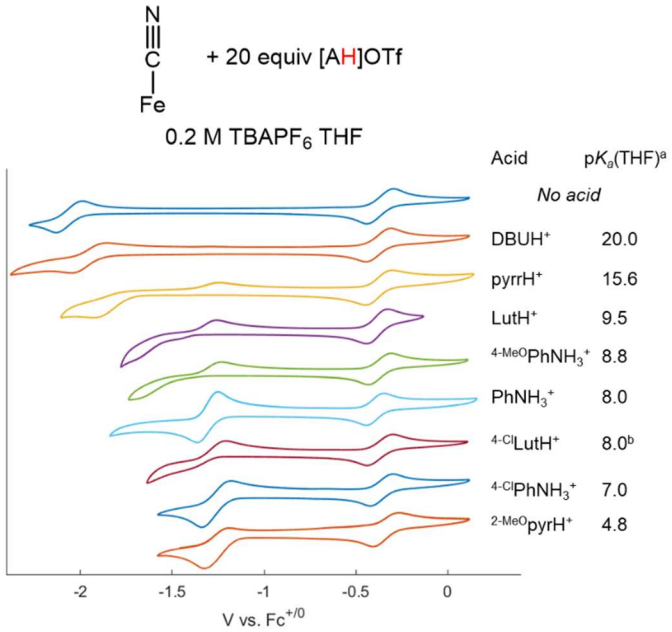

Figure B.63. Cyclic voltammetry of [FeCN] (1 mM, dashed lines) in 0.2 M [TBA]PF_6, in THF with added acid (20 mM [acid]OTf) at 100 mV s^{-1} scan rate. [a]pK_a from ref [10]; [b]pK_a measured in section B.9.

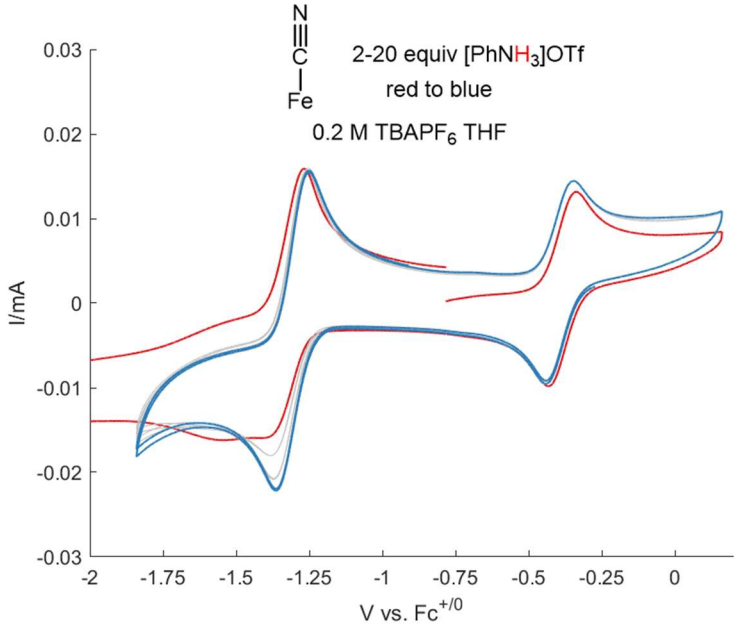

Figure B.64. Cyclic voltammetry of [FeCN] (1 mM, dashed lines) in 0.2 M [TBA]PF_6, in THF with added [$PhNH_3$]OTf (2 to 20 mM [acid]OTf).

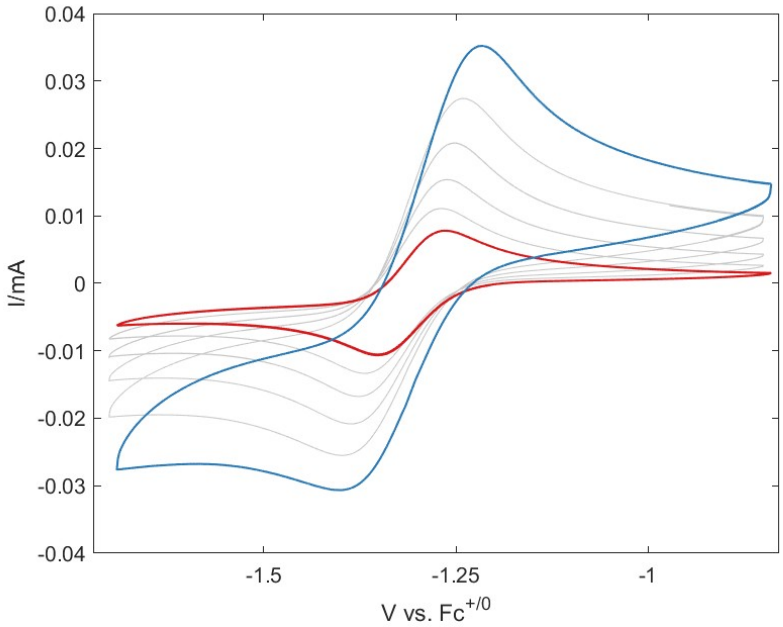

Figure B.65. Cyclic voltammetry of [FeCN] (1 mM, dashed lines) in 0.2 M [TBA]PF_6, in THF with added 20 mM [$PhNH_3$]OTf. Scan rate is varied from 25 mV s^{-1} to 800 mV s^{-1}.

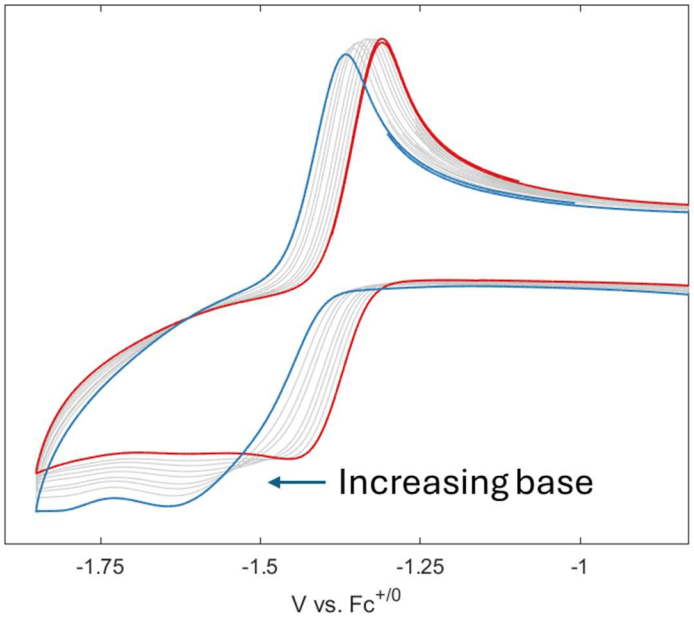

Figure B.66. Cyclic voltammetry of [FeCN] (1 mM, dashed lines) in 0.2 M [TBA]PF_6, in THF with added 20 mM [$PhNH_3$]OTf and varying amounts of [$PhNH_2$] (8 mM to 50 mM). Scan rate is 100 mV s^{-1}.

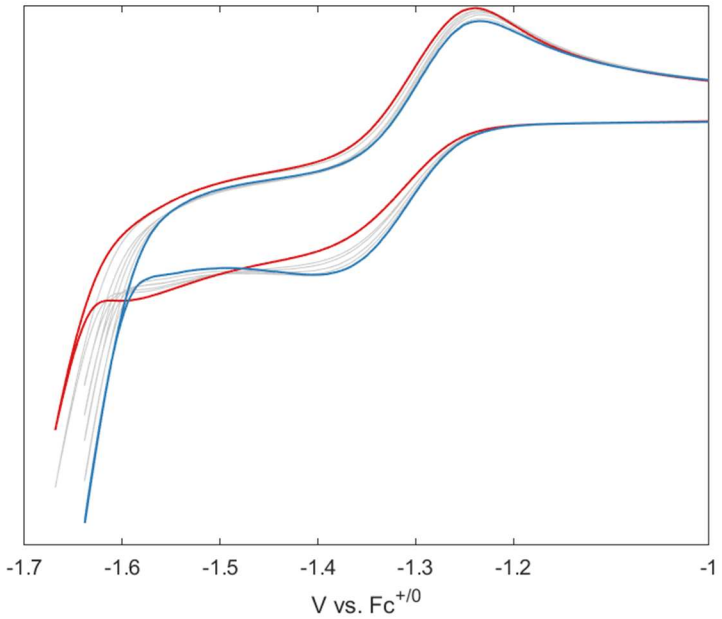

Figure B.67. Cyclic voltammetry of [FeCN] (1 mM, dashed lines) in 0.2 M [TBA]PF_6, in THF with added [$^{4\text{-Cl-2,6-Me}}$pyrH]OTf (10 to 60 mM; red to blue). Scan rate is 100 mV s^{-1}.

B.8.2 Additional comment on cyclic voltammograms of [FeCN] with acids

The differences observed between chemical (Figure 3.5) and electrochemical reductions (Figure B.63) are worth commenting on beyond the limited discussion in the main text. Monitoring chemical reduction of [FeCN] for a wide range of pK_a (7.0-15), the formation of the thermodynamically favored products is observed to occur rapidly, and in the case of Lut, equilibration is demonstrated. Monitoring the electrochemical reduction of [FeCN], we observe only strong acids (pK_a ~8) display reversible behavior. We attribute this to the weaker H-bonds formed under electrochemical conditions and a faster timescale of measurement that might disfavor sluggish reactions. In addition, for the oxidative half-wave, there is no shift of redox peaks with acid pK_a, suggesting that the oxidation of [$FeCNH_2$] is no longer redox-coupled, so only acids that for reduction of [FeCN] to [$FeCNH_2$] close to E([$FeCNH_2$]$^{+/0}$) might display a reversible $2H^+/2e^-$ wave.

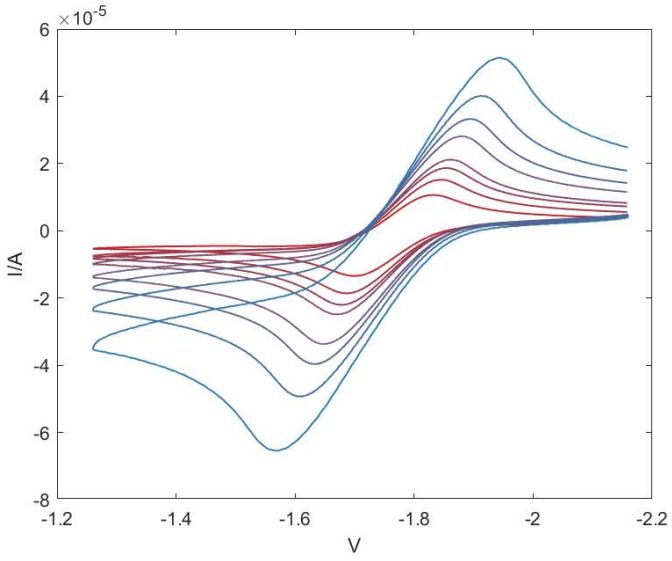

Figure B.68. Cyclic voltammetry of starting $^{Me4}Cp_2Co$ (1 mM, dashed lines) in 0.2 M [TBA]PF_6, in THF with varying scan rate from 25 (red trace) to 1000 mv s^{-1} (blue trace). Measured reduction potential measured as $E°$=−1.76 V vs $Fc^{+/0}$.

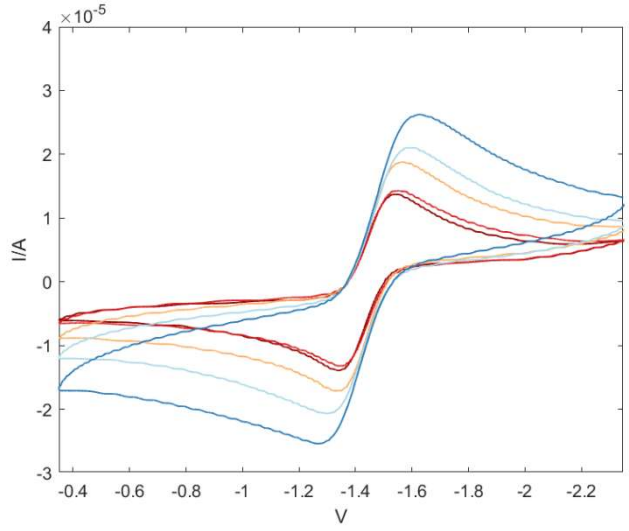

Figure B.69. Cyclic voltammetry of starting $^{Et}Cp_2Co$ (1 mM, dashed lines) in 0.2 M [TBA]PF_6, in THF with varying scan rate from 25 (red trace) to 1000 mv s^{-1} (blue trace). Measured reduction potential measured as $E°$=−1.45 V vs $Fc^{+/0}$.

B.9 Measurement of pK_a by NMR

B.9.1 General procedure

The acidity of $^{4\text{-Cl-2,6-Me}}$pyr had not been measured in THF. Given its central use in our discussion of the electrochemical reduction of [FeCN], we wanted to measure the acidity in THF against $PhNH_2$ to provide a tight and internally consistent comparison.

Using a method similar to what our group has previously used,[11] we started with an NMR tube with a known concentration of [$^{4\text{-Cl-2,6-Me}}$pyrH]OTf. Varying amounts of a $PhNH_2$ stock solution were added, and the shifts of ^{1}H NMR peaks were recorded. By comparing the position (as indicated in Figure B.70) to the acid (BH^+) and base (B) of the two components, we estimated the relative ratio of [acid]/[base] for both species.

$$[\mathrm{BH^+}] = \frac{(\delta_{obs} - \delta_{\mathrm{B}})}{(\delta_{\mathrm{BH+}} - \delta_{\mathrm{B}})} * [\mathrm{B}]_{tot} \quad \text{(eqn B.10)}$$

$$[\mathrm{B}] = [\mathrm{B}]_{tot} - [\mathrm{BH^+}] \quad \text{(eqn B.11)}$$

These values were used to estimate $K_{eq,\,exp}$ the equilibrium constant for each spectrum.

$$K_{eq} = \frac{[\mathrm{PhNH_3{}^+}][^{4-\mathrm{Cl}-\ ,6-\mathrm{Me}}\mathrm{Pyr}]}{[\mathrm{PhNH_2}][^{4-\mathrm{Cl}-2,6-\mathrm{Me}}\mathrm{PyrH^+}]} \quad \text{eqn (B.12)}$$

The average of these values was used to determine K_{eq} = 0.90±0.03 M^{-1}, which via the pK_a of $PhNH_2$ (pK_a 8.0),[10] allows us to determine the pK_a of $^{4\text{-Cl-2,6-Me}}$pyr.

$$p\mathrm{K_a}(^{4-\mathrm{Cl}-\ ,6-\mathrm{Me}}\mathrm{PyrH^+}) = p\mathrm{K_a}(\mathrm{PhNH_3{}^+}) - log_{10}(K_{eq}) \quad \text{eqn(B.13)}$$

$$= 8.0 - log_{10}(0.9) = 8.0$$

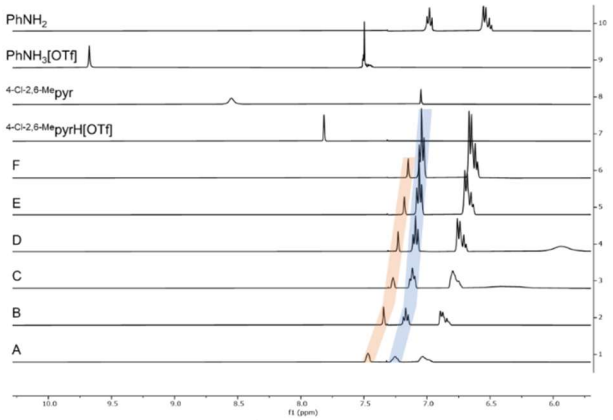

Figure B.70. Titration of [$PhNH_2$] in [$^{4\text{-Cl-2,6-Me}}$pyrH]OTf in THF as monitored by ^{1}H NMR. Peaks used to calculate acid/base ratio and positions of peaks in authentic acids and base are indicated as shown. Amount of [$PhNH_2$] added increases from A to F.

Note: All spectra were measured in h_8-THF with solvent suppression applied and with spectra shimmed on the ^{1}H peaks through the lock-channel.

Table B.4. Table with peak positions recorded based on Figure B.71 with subsequent amounts of titration components calculated along with $K_{eq,exp}$ and K_{eq} with associated error bars.

Entry	$PhNH_2$ added (equiv)	Vol. (mL)	^{1}H NMR pos. $^{4\text{-Cl-2,6-Me-}}$pyr (ppm)	Conc. $[^{4\text{-Cl-2,6-Me-}}$pyrH$]^+$ (mM)	Conc. $[^{4\text{-Cl-2,6-Me-}}$pyr] (mM)	^{1}H NMR pos. $PhNH_2$ (ppm)	Conc. $[PhNH_3]^+$ (mM)	Conc. $[PhNH_2]$ (mM)	$K_{eq,\ exp}$ (M^{-1})
Acid		0.6	7.82			7.50			
Base			7.05			6.98			
A	0.9	0.61	7.46	5.2	4.6	7.25	4.8	4.4	0.94
B	1.8	0.62	7.35	3.8	5.9	7.17	6.3	11.1	0.90
C	2.7	0.63	7.27	2.7	6.8	7.12	6.9	19.0	0.91
D	3.6	0.64	7.23	2.2	7.2	7.09	7.1	26.6	0.87
E	5.5	0.66	7.18	1.5	7.6	7.06	7.6	42.3	0.88
F	7.6	0.68	7.15	1.1	7.7	7.04	7.6	59.1	0.86

$K_{eq,\ exp}$ (M^{-1})	0.90
Error (M^{-1})	0.03

B.10 Computational studies and implementation of ECW model

B.10.1 General overview of computational details

For our computational studies we employed the TPSS functional[12] and a def2-TZVP basis set on transition metals and a def2-SVP basis set on all other atoms,[13] which we have previously demonstrated accurately replicate BDFEs on similar platforms.[14] The ORCA open source software package was used.[15] The numerical frequencies of the minimized structures were calculated to ensure that these structures represented local minima and not saddle points. The energies of relevant structures are displayed in Table B.6.

B.10.2 ECW model

The ECW model was used to classify the strength and type of Lewis basicity displayed by $P_3{}^BFeNN$, $P_3{}^BFeNNH$ and $P_3{}^BFeNNH_2$. Using the calculated gas phase enthalpies of the $P_3{}^BFeNN(H)_x\cdots LA$ (x = 0,1 or 2) adducts and the known C_A and E_A parameters of five Lewis acids (HNCS, PhOH, PhSH, BF_3 and BMe_3, see table B.6). A minimal solution was then found to these five simultaneous equations. An additional binding energy (ΔH_{disp}) of ~8 kcal mol^{-1}, a weak dispersive interaction, was also found as the Lewis acidity trended towards 0, this was accounted for as an additional parameter in the five simultaneously solved equations.

$$-\Delta H = C_A C_B + E_A E_B - \Delta H_{disp} \quad \text{eqn(B.14)}$$

The C_B and E_B parameters also allow us to compare $P_3{}^BFeNN(H)_x$ to other known Lewis bases, this is shown in Figure B.71.

With these determined values the Lewis adduct strength, we can also predict the $BDFE_{N\text{-}H}$ of stabilized diazenido and hydrazido complexes using eqn B.15

$$\mathrm{BDFE_{X-H\cdots LA}} = \mathrm{BDFE_{X-H}} + (\Delta H_{\mathrm{X-H}} - \Delta H_X) \quad \text{eqn(B.15)}$$

Table B.6. E_A and C_A parameters of Lewis acids used to determine E_B, C_B and ΔH_{disp} for $P_3{}^BFeNN$, P_3FeNNH and $P_3{}^BFeNNH_2$.

Lewis acid	E_A $(kcal\ mol^{-1})^{1/2}$	C_b $(kcal\ mol^{-1})^{1/2}$	W $(kcal\ mol^{-1})$
BF_3	6.1	2.87	0
BMe_3	2.9	3.6	0
PhOH	2.27	1.07	0
PhSH	0.58	0.37	0
HNCS	2.85	0.7	0

Table B.7. Computed E_B, C_B and ΔH_{disp} parameters for $P_3{}^BFeNN$, P_3FeNNH and $P_3{}^BFeNNH_2$.

Lewis base	E_A $(kcal\ mol^{-1})^{1/2}$	C_b $(kcal\ mol^{-1})^{1/2}$	ΔH_{disp} $(kcal\ mol^{-1})$
$P_3{}^BFeNN$	0.9±0.3	0.0±0.35	9.8
$P_3{}^BFeNNH$	2.8±0.4	0.4±0.7	8.7
$P_3{}^BFeNNH_2$	2.1±0.5	0.0±0.8	7.6

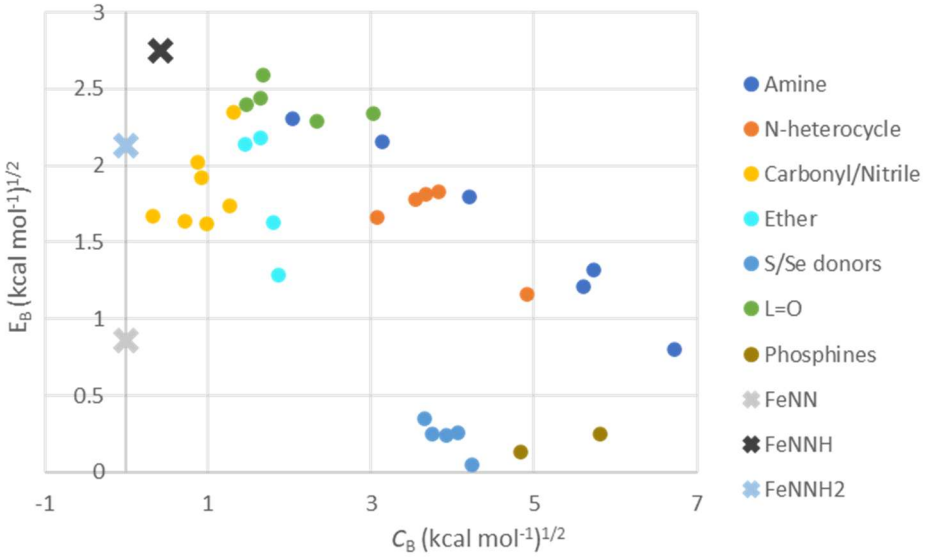

Figure B.71. Comparison of E_B and C_B parameters for $P_3{}^BFeNN$, P_3FeNNH and $P_3{}^BFeNNH_2$ with other Lewis bases.

Table B.8. Estimated $BDFE_{N-H}$ for Lewis acid stabilized adduct of $P_3{}^BFeNN$, P_3FeNNH and $P_3{}^BFeNNH_2$.

Lewis acid	BDFE(FeNNH) (kcal mol^{-1})	BDFE($FeNNH_2$) (kcal mol^{-1})
None	26.9	38.2
CH_2Cl_2	26.3	36.7
$HCCl_3$	27.2	36.2
^tBuOH	27.5	36.3
C_4H_4NH	27.6	36.1
$C_8H_{17}OH$	27.7	36.2
HNCO	27.7	36.0
HNCS	28.2	35.5
$(CH_3)_3SnCl$	28.2	35.5
CF_3CH_2OH	28.5	35.6
SO_2	28.8	36.0
$^{4\text{-Me}}PhOH$	28.5	35.6
PhOH	28.6	35.6
$^{4\text{-CF3}}PhOH$	29.0	35.4
cobalt(II) protoporhyrin IX dimethyl ester IX	29.1	35.4
I_2	29.6	35.7
$(CF_3)_2CHOH$	29.4	35.1
ZnTPP	29.5	35.1
ICl	30.0	34.9
$Cd[N(Si(CH_3)_2]_2$	30.1	35.0
$1/2[Pd(\pi\text{-ally})Cl]_2$	30.3	35.1
$(CF_3)_3COH$	30.4	34.8
$Zn[N(Si(CH_3)_3]_2$	31.1	34.6
$1/2[Rh(COD)_2Cl]_2$	31.4	34.6
$Cu(HFacac)_2$	31.7	34.7
IBr	32.2	34.6
$Ga(C_2H_5)_3$	31.2	33.4
$InMe_3$	32.3	33.2
BMe_3	33.5	33.8
$1/2[MeCo(Hdmg)_2]_2$	34.0	33
BF_3	33.4	32.9
$1/2[Rh(COD)_2Cl]_2$	35.0	32.9
$AlMe_3$	35.9	31.4
$SbCl_5$	46.1	29.4

B.11 X-ray crystallographic data

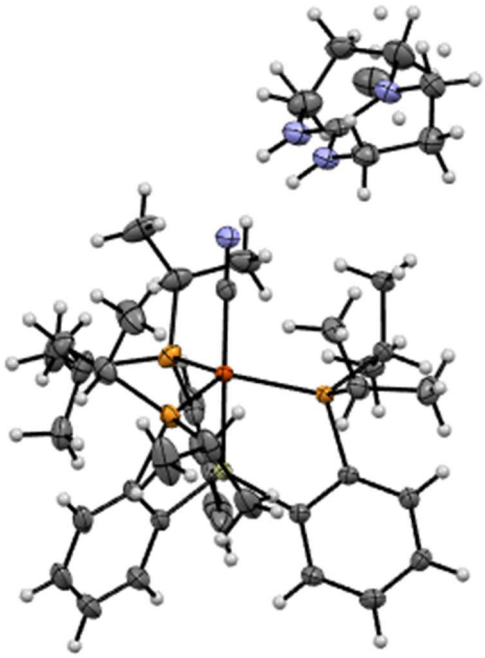

Figure B.72. ORTEP plot of [FeCN][HTBD] with H-atoms and disorder (in $TBDH^+$) shown.

Table B.9. Comparison of XRD parameters for [FeCN][HTBD] to [FeCN] species[1,2] and [TBDH]BPh_4.[16]

	[FeCN][HTBD]	[FeCN][$Na(12\text{-}c\text{-}4)_2$]	[FeCNMe]	[TBDH]BPh_4
C−N (Å)	1.172(3)	1.170(2)	1.186(2)	-
Fe−C (Å)	1.914(2)	1.949(2)	1.821(2)	-
Fe−P (Å)	2.2670(7)	2.252(1)	2.287(1)	-
Fe−P (Å)	2.2378(7)	2.231(1)	2.2729(8)	-
Fe−P (Å)	2.2353(6)	2.2242(4)	2.2560(7)	-
Mean (Fe-P) (Å)	2.2467	2.262067	2.271967	-
Fe−Si (Å)	2.2209(7)	2.242(1)	2.2732(8)	-
N_c-C (Å)	1.341(3)	-	-	1.328
N_a-C_d (Å)	1.328(3)	-	-	1.33
N_b-C_d (Å)	1.327(3)	-	-	1.33
$N_{a,TBD}$-N_{CN} (Å)	2.943(3)	-	-	-
$N_{b,TBD}$-N_{CN} (Å)	2.864(3)	-	-	-
<P-Fe-P °	131.04(2)	128.08(3)	122.87(2)	-
<P-Fe-P °	114.92(3)	114.11(3)	117.82(2)	-
<P-Fe-P °	108.58(2)	111.70(3)	112.49(2)	-
Σ<P-Fe-P	354.54	353.89	353.18	-
<Fe-C-N °	177.8(2)	177.4(2)	177.6(1)	-

Table B.10. Data relevant to crystal structure of [P_3^{Si}FeCN][HTBD].

Table 1 Crystal data and structure refinement for P_3^{Si}FeCN[HTBD]	
Identification code	
Empirical formula	$C_{42}H_{68}N_4SiP_3Fe$
Formula weight	805.85
Temperature/K	100.0
Crystal system	monoclinic
Space group	$P2_1/c$
a/Å	11.5710(4)
b/Å	18.3047(6)
c/Å	21.3059(7)
α/°	90
β/°	103.861(2)
γ/°	90
Volume/Å³	4381.3(3)
Z	4
ρ_{calc}g/cm³	1.222
μ/mm⁻¹	4.302
F(000)	1732.0
Crystal size/mm³	? × ? × ?
Radiation	CuKα (λ = 1.54178)
2Θ range for data collection/°	6.448 to 158.584
Index ranges	-14 ≤ h ≤ 14, -22 ≤ k ≤ 20, -26 ≤ l ≤ 26
Reflections collected	108896
Independent reflections	9339 [R_{int} = 0.0640, R_{sigma} = 0.0268]
Data/restraints/parameters	9339/0/501
Goodness-of-fit on F²	1.134
Final R indexes [I>=2σ (I)]	R_1 = 0.0418, wR_2 = 0.1316
Final R indexes [all data]	R_1 = 0.0493, wR_2 = 0.1402
Largest diff. peak/hole / e Å⁻³	0.46/-0.58

B.12 References for Appendix B

1. Rittle, J.; Peters, J. C. *Angew. Chem. Int. Ed.* **2016**. 55, 12262–12265.
2. Rittle, J.; Peters, J. C. *J. Am. Chem. Soc.* **2017**. 139, 3161–3170.
3. Del Castillo, T. J.; Thompson, N. B.; Peters, J. C. *J. Am. Chem. Soc.* **2016**. 138, 5341–5350.
4. Köhler, F. H.; Doll, K. *Z. Für Naturforschung B* **1982**. 37, 144–150.
5. Chalkley, M. J.; Del Castillo, T. J.; Matson, B. D.; Peters, J. C. *J. Am. Chem. Soc.* **2018**. 140, 6122–6129.
6. Fajardo, J.; Peters, J. C. *J. Am. Chem. Soc.* **2017**. 139, 16105–16108.

7. Fulmer, G. R.; Miller, A. J. M.; Sherden, N. H.; Gottlieb, H. E.; Nudelman, A.; Stoltz, B. M.; Bercaw, J. E.; Goldberg, K. I. *Organometallics* **2010**. 29, 2176–2179.
8. Stoll, S.; Schweiger, A. *J. Magn. Reson.* **2006**. 178, 42–55.
9. Perkampus, H.-H. *UV-VIS Spectroscopy and Its Applications*; Springer Science & Business Media, 2013.
10. Garrido, G.; Rosés, M.; Ràfols, C.; Bosch, E. *J. Solut. Chem.* **2008**, 37, 689–700. .
11. Chalkley, M. J.; Garrido-Barros, P.; Peters, J. C. *Science* **2020**. 369, 850–854.
12. Tao, J.; Perdew, J. P.; Staroverov, V. N.; Scuseria, G. E. *Phys. Rev. Lett.* **2003**, 91, 146401–146404.
13. Weigend, F. *Phys. Chem. Chem. Phys.* **2006**, 8, 1057–1065.
14. Matson, B. D.; Peters, J. C. *ACS Catal.* **2018**, 8, 1448–1455.
15. Neese, F.; Wennmohs, F.; Becker, U.; Riplinger, C. *J. Chem. Phys.* **2020**, 152, 224108.
16. Khalaf, M. S.; Oakley, S. H.; Coles, M. P.; Hitchcock, P. B. *CrystEngComm* **2008**. 10, 1653–1661.